



**HAL**  
open science

# On the high cycle fatigue resistance of austenitic stainless steels with surface gradient microstructures: Effect of load ratio and associated residual stress modification

Clément Dureau, Mandana Arzaghi, Roxane Massion, Yves Nadot, Thierry Grosdidier

## ► To cite this version:

Clément Dureau, Mandana Arzaghi, Roxane Massion, Yves Nadot, Thierry Grosdidier. On the high cycle fatigue resistance of austenitic stainless steels with surface gradient microstructures: Effect of load ratio and associated residual stress modification. *Materials Science and Engineering: A*, 2022, pp.142916. 10.1016/j.msea.2022.142916 . hal-03601305

**HAL Id: hal-03601305**

**<https://hal.univ-lorraine.fr/hal-03601305>**

Submitted on 9 Mar 2022

**HAL** is a multi-disciplinary open access archive for the deposit and dissemination of scientific research documents, whether they are published or not. The documents may come from teaching and research institutions in France or abroad, or from public or private research centers.

L'archive ouverte pluridisciplinaire **HAL**, est destinée au dépôt et à la diffusion de documents scientifiques de niveau recherche, publiés ou non, émanant des établissements d'enseignement et de recherche français ou étrangers, des laboratoires publics ou privés.

1 **On the high cycle fatigue resistance of austenitic stainless steels with surface gradient**  
2 **microstructures: effect of load ratio and associated residual stress modification**

3

4 Clément DUREAU<sup>1,2,3</sup>, Mandana ARZAGHI<sup>3</sup>, Roxane MASSION<sup>1,2</sup>, Yves NADOT<sup>3</sup>, Thierry  
5 GROSDIDIER<sup>1,2\*</sup>

6 <sup>1</sup> Université de Lorraine, Laboratoire d'Etude des Microstructures et de Mécanique des Matériaux, CNRS  
7 UMR 7239, 7 rue Félix Savart, 57073 Metz, France

8 <sup>2</sup> Université de Lorraine, LABoratoire d'EXcellence Design des Alliages Métalliques pour Allègement de  
9 Structures, 7 rue Félix Savart, 57073 Metz, France

10 <sup>3</sup> Institut Pprime, UPR 3346 CNRS- ISAE-ENSMA- Université de Poitiers, Téléport 2, 1 Avenue Clément  
11 Ader, BP 40109, 86961 Futuroscope Chasseneuil Cedex

12 \*Corresponding author: Thierry GROSDIDIER [thierry.grosdidier@univ-lorraine.fr](mailto:thierry.grosdidier@univ-lorraine.fr)

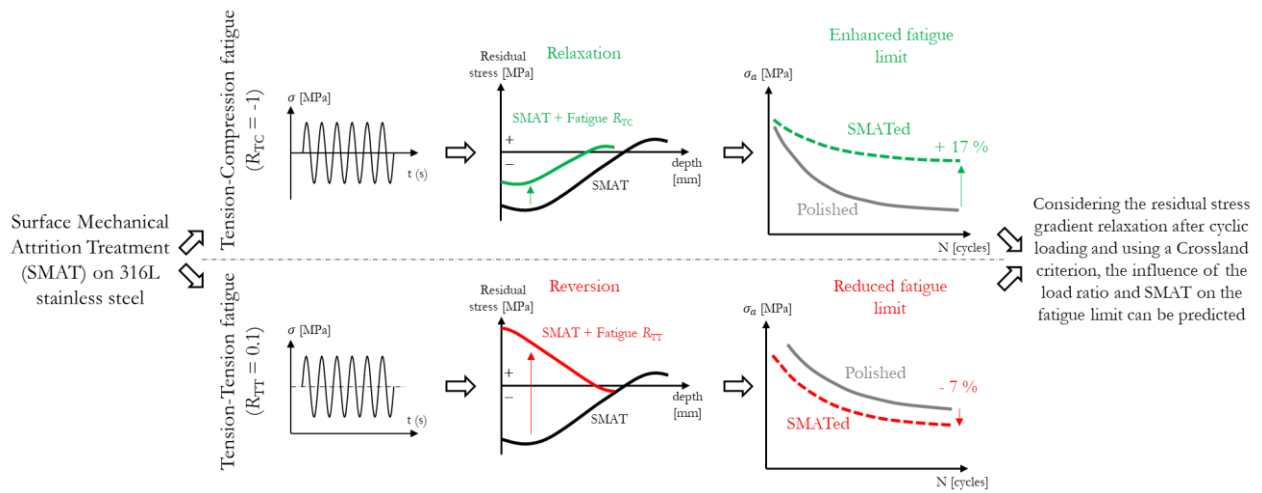
13 **Abstract**

14 The effect of gradient microstructure generated by ultrasonic surface mechanical attrition treatment (SMAT)  
15 on the fatigue performance of an austenitic stainless steel has been evaluated in the context of localized and  
16 general plasticity by comparing two load ratios: fully reversed tension-compression (TC)  $R_{TC} = -1$  and  
17 tension-tension (TT)  $R_{TT} = +0.1$ , respectively.

18 After identical SMAT processing conditions, the fatigue limit was enhanced by +17 % for  $R_{TC}$  while it was  
19 reduced by -7 % for  $R_{TT}$ . Under  $R_{TC}$  cyclic loading, self-heating of the specimens and sub-surface martensitic  
20 transformation occurred but not for  $R_{TT}$ . The residual stress measurements have also revealed that while the  
21 stress gradient was smoothed after the  $R_{TC}$  fatigue loading, it was completely reverted for the  $R_{TT}$  one. In turns,  
22 the fatigue crack initiation sites and propagation were modified between the  $R_{TT}$  and  $R_{TC}$  loading conditions.

23 Considering the stabilized surface residual stress after fatigue loading, the use of a Crossland criterion allowed  
24 to explain both the effects of load ratio and SMAT on the high cycle fatigue behavior of the stainless steel. It  
25 turns out that under the studied loading conditions the modifications of residual stress state can be considered  
26 as the primary factor governing the varying fatigue performances and the observed triggering at different  
27 initiation sites.

28 **Graphical abstract**



29

30 **Keywords:** Surface mechanical attrition treatment (SMAT), ultrasonic shot peening (USP), 316L austenitic  
 31 stainless steel, fatigue, load ratio, residual stresses

32 **1. Introduction**

33 In the last two decades, functionally graded materials (FGMs) have been broadly studied, particularly  
 34 those with varying properties from surface to core. In addition, such materials offer unique mechanical or  
 35 chemical properties through microstructure or hardening gradients. As a result, automotive, aeronautic, or  
 36 energy production industries expect them to produce higher efficiency and more reliable components [1, 2],  
 37 especially those subjected to fatigue issues.

38 In cases such as corrosion, friction wear, or fatigue for which the surface is a critical issue, surface  
 39 modifications may be sufficient to improve the properties of the mechanical part. In terms of fatigue, as most  
 40 cracks initiate from the surface, inducing a compressive residual stress state by shot peening improves the  
 41 fatigue limit of a wide variety of materials [3-7]. Also, surface severe plastic deformation (SPD) processes that  
 42 lead to FGMs having an ultrafine grain (UFG) surface microstructure represent a way to enhance the functional  
 43 properties of materials. Among those processes, surface mechanical attrition treatment (SMAT) or ultrasonic  
 44 shot peening (USP) are derived from conventional shot peening (CSP) [8-12]. They differ from CSP because  
 45 the motion of the shots is made within a confined chamber so that the shots can impact the surface of the  
 46 sample, by colliding and bouncing on the chamber walls, for a potentially longer time and with a wider range  
 47 of incidence angles. This leads to an increased number of activated slip systems allowing to very effectively  
 48 refine the microstructure leading to a UFG state at the surface and the formation of a gradient

49 microstructure [13, 16]. SMAT or similar treatments were suggested to be efficient ways to enhance the fatigue  
50 behavior of many metallic alloys due to the coupled effect of microstructure, hardening gradient, and  
51 compressive residual stresses [17-22]. However, some manuscripts suggested that SMAT can be detrimental  
52 for some materials or if the chosen set of parameters for the SMAT treatment is not optimized [23-27].

53         The 316L stainless steel is an example of highly used austenitic steel that, despite its good oxidation  
54 and corrosion resistances as well as its good formability, suffers from moderate mechanical properties.  
55 Different strengthening processes have been studied as a way to improve the mechanical properties of such  
56 alloys without giving up too much of their other characteristics [28-30]. By inducing hardening, residual  
57 stresses, and UFG microstructure layer, SMAT or similar processes have also been suggested to improve the  
58 fatigue behavior of 316L stainless steel. Indeed, Masaki et al. measured a nearly 100 % increase of the fatigue  
59 limit of 316L samples after hard shot-peening (HSP) when loaded in rotating bending [31]. Uusitalo et al. [18]  
60 and Roland et al. [32] respectively observed an 83 % and 21 % higher fatigue limit after performing SMAT  
61 with 3 mm diameter beads on 316L. Comparatively, with similar SMAT treated 316L samples, Sun et al.  
62 highlighted that the number of cycles to failure was unchanged compared to the untreated ones in the low cycle  
63 fatigue (LCF) regime despite the enhanced stress amplitudes for the SMAT-processed specimens [33]. Here  
64 again, on austenitic stainless steels, the literature gives apparently conflicting results. This unchanged fatigue  
65 life was proposed to be due to the higher residual stress relaxations induced by the higher strain amplitudes in  
66 LCF than in high cycle fatigue (HCF). This was then further investigated by Sun et al., who reported an almost  
67 fully relaxed residual stress gradient after a fatigue test conducted at 1.25 % of strain amplitude [34].  
68 Huang et al. even measured a slight tensile residual stresses gradient after 3 % strain [35]. Therefore, this  
69 suggests that the macroscopic plastic strains could be affecting the residual stress gradient relaxation after  
70 fatigue loading, and then the fatigue life of SMAT processed samples. But, most of the fatigue testing available  
71 in the literature [30, 32, 35] have been conducted in fully reversed loading condition ( $R = -1$ ), and as in this  
72 configuration the measured fatigue limits were in the same range of magnitude as the yield strength of the  
73 material, no data about the effect of macroscopic strain on the HCF behavior of SMAT processed 316L are  
74 available.

75         Thus, the goal of the present work is to shed some light on the exact capability of the SMAT to enhance  
76 the high cycle fatigue behavior for different loading conditions by taking the well-known commercial 316L  
77 stainless steel as a good test subject. Special attention will be paid to the effect of surface roughness and, as the

78 applied load ratio directly influences the macroscopic strains, to the evolutions of hardness and residual stress  
79 redistributions after fatigue loading.

## 80 2. Materials and Methods

### 81 2.1. Sample preparation and surface treatment

82 The studied material was an AISI 316L stainless steel formed by swaging above 1040 °C into a 20 mm  
83 diameter bar. Table 1 summarizes the chemical composition of this steel together with the resulting martensite  
84 start temperature  $M_S$  and the  $M_{d30}$  temperature at which 50 % of martensite is formed when the material is  
85 subjected to a 30 % true strain. A heat treatment of 40 min at 900 °C was done on this raw material, resulting  
86 in a homogeneous microstructure with an average grain size of approximately 30  $\mu\text{m}$ . Tensile tests revealed a  
87 yield stress  $\sigma_{ys} = 220$  MPa, an ultimate tensile stress  $\sigma_{UTS} = 650$  MPa and an elongation to failure of 105 %.  
88 Fatigue specimens with a 9 mm diameter and a 12.5 mm gauge length were machined. In order to remove the  
89 plastically deformed and heat-affected zone induced by machining, a layer of about 75  $\mu\text{m}$  was removed by  
90 grinding the samples before polishing them to a mirror finish surface. While half of the polished samples were  
91 kept in this condition (initially polished condition – Table 2 a), the other half was treated by SMAT (SMAT  
92 condition – Table 2 a). The treatment was carried at a hitting distance of 20 mm for 60 min using a SONATS  
93 ultrasonic shot peening device [36] equipped with a sonotrode made of Ti-6Al-4V that was vibrating at a 60  $\mu\text{m}$   
94 amplitude and a 20 kHz frequency. A total of 4.1 grams of brand new 2 mm diameter 100C6 beads were  
95 inserted in the dedicated polyoxymethylene chamber before each treatment and two samples were treated  
96 simultaneously. The samples were rotated at a speed of 20 revolutions per minute during this surface  
97 mechanical attrition treatment. For specific analysis that will be described later on, some of these SMATed  
98 samples were mirror polished after a delicate grinding procedure with 1000 grit SiC abrasive  
99 paper (SMAT + polished condition – Table 2 a), resulting in a removed thickness of approximately 35  $\mu\text{m}$ . All  
100 the above-mentioned surface conditions are gathered in Table 2 a with their respective surface roughness.

### 101 2.2. Fatigue tests

102 The fatigue tests were load-controlled to evaluate the overall HCF performance of the studied material  
103 for different load ratios. The load ratio is defined by Equation (1), and in order to study its effect on the uniaxial  
104 fatigue behavior of the polished and SMAT states of the 316L stainless steel, both tension-compression (TC)  
105 and tension-tension (TT) fatigue tests were conducted.

106 
$$R = \sigma_{\min} / \sigma_{\max} \quad (1)$$

107 The following values of the load ratio were selected:  $R_{TC} = -1$  and  $R_{TT} = +0.1$ . The fatigue tests were carried out  
108 at room temperature at a loading frequency of 10 Hz with an 810MTS servo-hydraulic machine. Any sample  
109 reaching  $10^6$  cycles without breaking was considered a run-out and was not reused.

110 2.3. Samples characterization

111 Fracture surfaces of the broken samples were analysed using optical microscopy (OM) and scanning  
112 electron microscopy (SEM) to reveal the differences in crack initiation and propagation between the different  
113 tested conditions.

114 In order to decorrelate the influence of the gradients of microstructure, hardness, and residual stresses,  
115 reference SMATed samples were compared to the run-out samples that experienced the highest fatigue tested  
116 stress amplitude under  $R_{TC}$  and  $R_{TT}$  without failure. They were denominated as “SMAT + Fat  $R_{TC}$ ” and  
117 “SMAT + Fat  $R_{TT}$ ”. A final condition was studied, for which a SMATed sample was tested for one single cycle  
118 at  $R_{TT}$  at the same stress level as the SMAT + Fat  $R_{TT}$  one. This sample was analysed to learn about the effect  
119 of the number of fatigue cycles; it was named “SMAT + 1Cy  $R_{TT}$ ”. The testing conditions and their labelling  
120 are gathered in Table 2 b. For these four conditions (SMAT, SMAT + Fat  $R_{TC}$ , SMAT + Fat  $R_{TT}$  and  
121 SMAT + 1Cy  $R_{TT}$ ), the hardening state characterization was done by standard HV 0.3/20 Vickers micro-  
122 hardness measurements. They were conducted on specimen cross sections perpendicularly to the SMAT layer  
123 starting 30  $\mu\text{m}$  below the surface until reaching the core material. Each indent was spaced by 100  $\mu\text{m}$  to avoid  
124 interference, and 10 measurements were conducted for each given depth. In parallel, the in-depth residual stress  
125 gradients before and after fatigue loading of those four samples were characterized by X-ray diffraction after  
126 successive material layer removal using electrochemical polishing. For electro-polishing, a solution consisting  
127 of a mix of 6 % perchloric acid, 35 % butoxyethanol and 59 % methanol was used. The cylindrical fatigue  
128 samples were rotated during the XRD measurement to increase the number of diffracting grains and average  
129 potential local effects. A Pulstec  $\mu$ -X360s device with a mounted Cr tube operating at 30 kV and 1.5 mA  
130 allowed to obtain full diffraction rings from the two-dimensional detector. The “Analysis Tools for Electron  
131 and X-ray diffraction” (ATEX) software [37], developed in LEM3, was used for post-processing the acquired  
132 data using the “cos  $\alpha$ ” method. Finally, due to the residual stress redistribution occurring during successive  
133 material layer removal, the experimentally measured gradient was corrected using the Moore and Evans  
134 relations [38].

### 135 3. Results

136 The results will be presented hereafter into different subsections. The first subsection gathers the  
137 fatigue test results. Fatigue tests were carried out at  $R_{TC}$  for both the polished and SMAT conditions to set the  
138 reference data for easier comparison with the literature. Then similar tests were conducted at  $R_{TT}$  in order to  
139 highlight the effect of the load ratio. The second subsection details the analysis of the fracture surfaces. The  
140 third subsection deals with the analysis of the run-out samples. First, the surface of the run-out samples were  
141 investigated using SEM to look for potential fatigue cracks. Also, residual stress as well as hardness evolutions  
142 were studied to get further information about the material behavior in the fatigue limit regime of the SMATed  
143 samples for both  $R_{TC}$  and  $R_{TT}$ . Finally, this result section will be concluded by a Crossland initiation criterion  
144 analysis taking into account the relaxed residual stress fields to analyse the combined effects of load ratio and  
145 SMAT.

#### 146 3.1. Fatigue properties

147 Figure 1 gives the Wöhler curves obtained for the polished and the SMAT conditions for both testing  
148 conditions: TC in Figure 1 a and TT in Figure 1 b. Circles represent the polished samples while the squares  
149 and stars the SMAT and SMAT + polished conditions, respectively. The full and hollow symbols indicate the  
150 broken and run-out specimens, respectively. The experimental data were fitted using the Stromeier  
151 equation [39] defined by Equation (2), a full line was used for fitting the polished state and a dotted line for the  
152 SMAT one, while the SMAT + polished data were not fitted due to the small number of tested specimens.

$$153 \quad \sigma_a = \sigma_D + \left(\frac{c}{N}\right)^{(1/m)} \quad (2)$$

154 In Figure 1 a, the results obtained by Dureau et al. in a previous study on the 304L stainless steel [40] were  
155 superimposed. Indeed, the data reported in Figure 1 a show that the 304L and 316L samples exhibit very  
156 similar fatigue behavior for both surface conditions.

157 For the Wöhler curves of the samples loaded at  $R_{TC}$  (Figure 1 a), the fatigue limits are estimated to be  
158 205 MPa and 240 MPa for the polished and SMAT conditions, respectively. Clearly, the SMAT provided an  
159 increase of about +17 % of the fatigue limit at  $R_{TC}$ . For this  $R_{TC}$  loading condition, self-heating of the surface  
160 of the specimens as high as 150 and 250 °C was measured for the highest tested stress amplitudes for the  
161 polished and SMATed samples respectively. For the samples loaded in the range of the fatigue limit, the  
162 self-heating was less than 50 °C and considered negligible, similarly to what was reported in a previous

163 work [40]. For the  $R_{TT}$  loading, Figure 1 b indicates that the fatigue life of the SMATed samples was very  
164 similar to the polished ones in the  $10^5$  cycle regime, while it tended to be slightly lower in the  $10^6$  cycle domain.  
165 Under  $R_{TT}$ , the fatigue limits were estimated to be 230 MPa and 215 MPa for the polished and SMAT  
166 conditions, respectively. Comparatively, for the SMAT + polished specimens also loaded at  $R_{TT}$ , the fatigue  
167 life as well as the fatigue limit of those specimens appeared to be slightly increased compared to the SMATed  
168 ones due to the post-polishing procedure. Contrary to what was observed for the  $R_{TC}$  condition, a reduction of  
169 about -7 % is induced by the surface mechanical attrition treatment when the samples are loaded at  $R_{TT}$ . The  
170 initially polished and SMAT + polished data almost superimpose for the  $R_{TT}$  conditions. This indicates that the  
171 actual surface state has an influence since the post-polishing procedure restored the overall fatigue properties.  
172 Interestingly, contrary to what was reported at  $R_{TC}$ , no self-heating of the specimens was measured for this load  
173 ratio.

### 174 3.2. Broken samples analysis

175 Figure 2 presents typical SEM images of the characteristic initiation sites observed on the different  
176 tested specimens. In Figure 2, the three horizontal lines correspond to the surface state of the samples (initial  
177 polished, SMAT, or SMAT + polished) while the columns rank the observations made for the two load ratios,  
178  $R_{TC}$  or  $R_{TT}$ , with images of samples that broke under high or low stress amplitudes.

179 For the  $R_{TC}$  loaded samples, the comparative analysis of the fracture surfaces - at a given stress  
180 amplitude for the polished and SMAT conditions - revealed very similar fatigue crack initiation features. As  
181 marked by the red arrows in Figure 2 a1, the high stress amplitude is witnessed by the presence of a secondary  
182 crack intercepting the fracture surface in the vicinity of the initiation site of the polished sample. For the SMAT  
183 samples subjected to a high stress amplitude, as illustrated in Figure 2 b1, no such crack was observed; instead,  
184 a very distinct river line aspect was revealed. For the low stress amplitude conditions, as shown in Figures 2 a2  
185 and b2, no difference was noticed on the initiation sites regardless of the surface condition. Thus, the observed  
186 modification of the crack initiation was more influenced by the applied stress amplitude than by the exact  
187 nature of the surface.

188 For the samples loaded at  $R_{TT}$  at high stress amplitudes, all the samples experienced fatigue crack  
189 initiation on surface inclusions whatever the exact nature of the surface condition as seen in Figures 2 c1, d1  
190 and e1. Moreover, all the observed inclusions exhibited a rather circular shape except for the SMAT conditions.  
191 Indeed, compared to the round solid inclusion shown in Figure 2 c1 for the polished sample, the inclusion seen



192 in Figure 2 d1 for the SMAT sample exhibits numerous sharp angles and facets. Indeed, in the case of rather  
193 large particles located at or just beneath the surface, the repeated impacts can result in their fragmentation  
194 directly under the action of SMAT. This can explain why fragmented inclusions were observed in some SMAT  
195 samples (Figure 2 d1) but not in the polished ones (Figure 2 c1). Figures 2 e1 highlights, once again, an  
196 initiation on a surface solid inclusion for the SMAT + polished condition; even if the inclusion was even ejected  
197 from the fracture surface for this specific sample, leaving a cavity. For the lowest stress amplitudes, initiation  
198 also occurred at the surface for the three conditions. However, inclusions were never observed at the initiation  
199 site of the analysed initial polished and SMAT conditions. Figure 2 c2 demonstrates that, as no inclusion is  
200 found, fatigue cracks are probably initiated on surface roughness induced by plasticity such as slip bands. In  
201 contrast, Figure 2 d2 shows that for the SMAT, initiation occurred on a dimple (i.e., a surface asperity induced  
202 by SMAT), as will be confirmed in Figure 3. For the SMAT + polished samples loaded at low  
203 stress (Figure 2 e2), initiation occurred at a surface inclusion as previously described for the  $R_{TT}$  high stress  
204 conditions. However, due to the lower number of tested samples, it seems speculative to conclude that no  
205 change in the initiation mechanism is observed when reducing the stress amplitude in the case of  
206 SMAT + polished samples.

207 Figure 3 gathers the EDX maps corresponding to the four areas surrounded by red rectangles in  
208 Figure 2. Only the case of  $R_{TT}$  samples is presented because the analysis carried out on the initiation sites of  
209 the  $R_{TC}$  samples did not reveal any inclusion or chemical heterogeneity. As shown in Figure 3 a, the inclusion  
210 found at the initiation site of the polished sample loaded at high stress amplitude is a rather complex calcium-  
211 aluminate oxide also containing magnesium. The inclusion visible in Figure 2 e2 for the case of a low stress  
212 SMAT + polished sample loaded at  $R_{TT}$  was another calcium aluminate oxide containing magnesium and  
213 silicon. The inclusions could also be simple aluminium oxides, as shown in Figure 3 b for a SMAT sample  
214 loaded at high amplitude. The most probable explanation for the presence of these different oxides is that they  
215 are initially formed between the molten metal and the slag by the addition of deoxidation products during the  
216 argon oxygen decarburation process. As explained by Zhang et al. [41], this usually leads to the formation of  
217 characteristic oxides based on  $\text{SiO}_2$ ,  $\text{CaO}$ , and  $\text{Al}_2\text{O}_3$ . These oxides being solid in the molten metal due to their  
218 higher melting temperature, they are present in the final product as inclusions of different oxide chemistry.  
219 These observed inclusions have a fairly nodular shape with a diameter of about 10  $\mu\text{m}$  regardless of their  
220 composition. On the other hand, Figure 3 c reveals that the dimple defect observed in Figure 2 d2 is filled by  
221 aluminium, titanium, and vanadium. This chemical composition corresponds to the characteristic

222 contamination layer that can form during sufficiently long surface mechanical attrition treatment. Such type of  
223 contamination layer is known to form by erosion ablated scraps coming from the 100C6 shots, the Ti-6Al-4V  
224 sole of the sonotrode or even particles from the chambers. Such contamination layer was already observed by  
225 Samih et al. and was even shown to reach depths of approximately 5  $\mu\text{m}$  due to the pile-up, ablation, and  
226 deposition mechanisms for similar SMAT conditions [42]. These observations were later confirmed by  
227 Chemkhi et al. on SMATed 316L stainless steel [43]. This contamination layer is known to affect the reactivity  
228 and corrosion resistance of the SMAT treated surfaces [10]. Its chemistry was also shown to have determining  
229 consequences regarding the wear behavior of the shot peened surfaces due to its effect on the exact nature of  
230 the abrasive oxides that form during dry contact friction [44].

231 Figure 4 compares the macroscopic optical observations of the fracture surfaces of the different tested  
232 specimen conditions (line a) with sketches of the fracture sequence with topology of these fracture surfaces  
233 (line b). For the  $R_{TT}$  loading conditions, the observed features for the SMAT and the SMAT + polished samples  
234 were similar; thus, only the SMAT condition is shown. For the  $R_{TC}$  loading condition of the polished sample  
235 (Figure 4 a1), the observation shows a fairly straight propagation front perpendicular to the propagation  
236 direction (i.e., sample radius) before the final fracture. Comparatively, the propagation region forms an internal  
237 circular-like area for the SMAT samples (Figure 4 a2). The same behavior was observed in a previous study  
238 on a 304L stainless steel treated by SMAT and loaded at  $R_{TC}$  [40]. For the  $R_{TT}$  loading conditions (Figure 4 a3  
239 and a4), semi-circular crack fronts were observed before the occurrence of a ductile fracture for all conditions.  
240 At this scale, no obvious difference in the shape of the fracture surfaces was observed when comparing the  
241 different polished and SMAT samples loaded at  $R_{TT}$ . Figures 4 b1, b2, b3, and b4, give the topology of the  
242 fracture surfaces and the initiation site was taken as the reference point for the measured altitude. The  
243 propagation plateau in the case of the  $R_{TC}$  polished sample is perfectly perpendicular to the loading axis, as  
244 indicated in Figure 4 b1 by the large domain of blue colour pointed by the red arrow. Comparatively, in the  
245 central region of the fracture surface of the  $R_{TC}$  SMAT sample, a slight angle of about  $7^\circ$  was observed  
246 perpendicular to the crack propagation direction due to the higher stress amplitude, as shown in Figure 4 b2.  
247 In addition as indicated by the dotted black arrows, the fatigue fracture surface delimited by the circle-like  
248 dotted line in Figure 4 b2 continued toward the hardened surface by a propagation zone inclined at  $45^\circ$ . Minor  
249 differences can be noticed on the fracture surfaces when comparing the  $R_{TT}$  conditions (Figures 4 b3 and b4).  
250 However, inclined propagation zones are visible in the vicinity of the surface for the shot peened samples, as  
251 outlined in Figure 4 b4 by the regions delimited by the curved dotted lines and pointed by the red arrows. These

252 specific crack propagation features for the SMAT samples loaded at  $R_{TC}$  and  $R_{TT}$ , because they were not visible  
253 for the initial polished samples, are then linked to the presence of the SMAT affected layer. They can either  
254 result from the microstructure and especially texture effects, as was already discussed for several UFG metallic  
255 materials such as interstitial-free steel [45], aluminium alloy [46], or commercially pure copper [47]. As the  
256 texture modifications under SMAT are rather weak [48], the modifications in crack propagation are more likely  
257 due to the tri-axial field of residual stress generated in this region. It leads to a curved crack propagation path,  
258 as discussed by Cotterell and Rice [49]. As shown by comparing Figures 4 b1, b2, b3, and b4, the failure  
259 sequence always consists of three stages. For all conditions, it starts with a surface crack initiation followed by  
260 a propagation phase and finishes with a ductile fracture. However, as confirmed by the larger domains of grey  
261 contrast in Figures 4 b3 and b4, the ductile fracture occurred after much shorter fatigue crack propagation for  
262 the  $R_{TT}$  than for the  $R_{TC}$  ones (Figures 4 b1 and b2). This is expected since, for an identical stress amplitude,  
263 the maximum macroscopic stress is more than twice as high for the  $R_{TT}$  loading condition than for the  $R_{TC}$  one.  
264 Also, due to this much higher stress while breaking, samples loaded at  $R_{TT}$  experienced necking and bending,  
265 leading to a much more deformed final section (Figures 4 b3 and b4) compared to the  $R_{TC}$  samples for which  
266 the original circular section can still be clearly distinguished (Figures 4 b1 and b2).

### 267 3.3. Unbroken samples analysis

268 Figure 5 presents the characteristic surface state of the run-out samples observed by SEM. ~~For  $R_{TC}$  the~~  
269 ~~images are not presented because, for the polished samples, the observation only revealed fine witness marks~~  
270 ~~of plastic activity while, for the SMAT samples, observation was nearly impossible due to the roughness of the~~  
271 ~~surface and the presence of the contamination layer (previously discussed in Figure 3 e) partially covering the~~  
272 ~~sample surface.~~ For  $R_{TC}$ , Figure 5 a reveals fine witness marks of plastic activity visible on the polished  
273 surface. Some favourably oriented grains exhibit slip bands which usually are parallel. Such traces were not  
274 visible for the SMAT samples (Figure 5 b) due to the roughness of the surface and the presence of the  
275 contamination layer (previously discussed in Figure 3 c) partially covering the sample surface. For  $R_{TT}$ , as  
276 shown in Figure 5 c, the surface of the polished samples is very affected by the fatigue loading. Indeed, it is  
277 covered with highly pronounced slip bands and the deformation of the grains creates a micro-roughness leading  
278 to the classic “orange-peel” aspect of the deformed samples. For the  $R_{TT}$  loaded SMAT samples, Figure 5 d  
279 illustrates that the contamination layer covering the SMAT sample surface is not homogeneous. Indeed, in  
280 Figure 5 d, the yellow dashed curve delimits the left end side where the rough surface of the fatigue sample is  
281 visible from the right end side where the contamination layer appears in a darker colour. Once again, the rough

282 SMAT surface does not allow to identify surface plasticity. Comparatively, as indicated by the red arrows, it  
283 is interesting to notice that the contamination layer of the samples has fractured during the fatigue loading due  
284 to the elongation of the stainless steel substrate. For the SMAT + polished condition, slip bands are visible at  
285 the surface of the samples (Figure 5 e). However, due to the refined microstructure generated during SMAT,  
286 the slip bands are not as straight as for the initial polished state. Figure 5 has shown that different surface states  
287 and plastic activity were identified for the different studied conditions. Nevertheless, fatigue crack initiation  
288 was never detected for run-out samples regardless of their surface condition or the imposed stress amplitude  
289 and load ratio. This indicates that initiation seems to be the key aspect to consider when studying the effect of  
290 SMAT on the HCF behavior of stainless steel.

291 Figure 6 gives the evolutions of the longitudinal component of the residual stress tensor with respect  
292 to the depth below the surface for different conditions. Figure 6 a compares the stress gradient after fatigue on  
293 a run-out sample for the  $R_{TC}$  loading (SMAT + Fat  $R_{TC}$  condition for  $\sigma_a = 240$  MPa) with the reference SMAT  
294 one. Figure 6 b shows the evolutions of the stress state for  $R_{TT}$  loading after one cycle (SMAT + 1Cy  $R_{TT}$  for  
295  $\sigma_a = 215$  MPa) and after another fatigue run-out (SMAT + Fat  $R_{TT}$  also for  $\sigma_a = 215$  MPa). The reference  
296 SMAT sample characterization is presented by solid black curves, while dotted and dashed lines are used after  
297 loading. As the 316L stainless steel samples underwent stress- or strain-induced martensitic phase  
298 transformation during the SMAT process, two phases did coexist. Thus, in the graphs, circles are the measured  
299 values of residual stress in austenite ( $\gamma$ ), while squares are used for martensite ( $\alpha'$ ). The error bars represent  
300 the standard deviation of each linear fit used in the “cos  $\alpha$ ” method for each measured point. For clarity, they  
301 are only displayed when the standard error is more than 50 MPa. As shown by the solid black curves in  
302 Figures 6 a and b, SMAT allowed to create a compressive residual stress gradient along about 600  $\mu\text{m}$  below  
303 the treated surface. Due to the stress and strain fields, a partial martensitic transformation occurred in the first  
304 100  $\mu\text{m}$  below the surface. This is rather consistent with the observations of Novelli et al. on the 304L stainless  
305 steel [50], even if it has to be recalled that the austenite in the 304L is less stable and then more susceptible to  
306 undergo martensitic transformation than for the 316L. For the reference SMAT condition, surface residual  
307 stresses of approximately -600 MPa and -900 MPa were evaluated in austenite and martensite, respectively.  
308 The maximum values of residual stresses were recorded slightly below the surface. They were -750 MPa for  
309 austenite at 100  $\mu\text{m}$  below the surface and -1 GPa for martensite at a depth of 25  $\mu\text{m}$ . These results are  
310 consistent with observations made by different authors [34, 40, 51]. Interestingly, after fatigue, stress  
311 relaxation took place in very different ways depending on the loading conditions. As shown in Figure 6 a for

312 the  $R_{TC}$  loading, the surface stresses were relaxed by approximately 50 % in both austenite and sub-surface  
313 martensite for the SMAT + Fat  $R_{TC}$  sample. This resulted in approximately constant internal stress levels along  
314 the first 100  $\mu\text{m}$  below the surface with values of -250 MPa and -500 MPa in the austenite and martensite  
315 phases, respectively. In addition to this compressive residual stress relaxation, the depth of the gradient was  
316 also reduced down to 275  $\mu\text{m}$ . Moreover, it is very interesting to notice that additional martensite was created  
317 during the cyclic loading at depths below 200  $\mu\text{m}$  (down to about 350  $\mu\text{m}$  because deeper investigations were  
318 not conducted). Thus, due to the load condition of SMAT followed by fatigue at  $R_{TC}$ , martensite was present  
319 in a fair amount at depth in the range 0-100  $\mu\text{m}$  and below 200  $\mu\text{m}$  but not detected in the 100-200  $\mu\text{m}$  depth  
320 domain. For the  $R_{TT}$  loading conditions, a reversion of the residual stress state was revealed. Indeed, for the  
321 SMAT + Fat  $R_{TT}$  sample, surface stresses of +850 MPa and +1250 MPa were measured in austenite and  
322 martensite, respectively. Similarly to what was observed on the SMAT + Fat  $R_{TC}$ , the residual stresses stored  
323 in martensite were relatively constant but, in this case, no additional stress- or strain-induced martensite was  
324 formed in the subsurface. In austenite, the internal stress level decreased almost linearly as a function of depth  
325 down to 350  $\mu\text{m}$  below the surface. Interestingly, the stress gradient was almost completely reverted after only  
326 one cycle of  $R_{TT}$  fatigue. Indeed, surface stress of +750 MPa in austenite and +1150 MPa in martensite were  
327 measured for the SMAT + 1Cy  $R_{TT}$  sample.

328 Figure 7 compares the SMAT reference hardness gradient with the ones measured after the different  
329 loading conditions. Figures 7 a, b, and c present the results for the SMAT + Fat  $R_{TC}$ , SMAT + Fat  $R_{TT}$ , and  
330 SMAT + 1Cy  $R_{TT}$  samples, respectively. Each point represents the average value and the error bars are the  
331 minimum and maximum hardness values measured at the corresponding depth. The hardness gradient for the  
332 reference SMAT sample before fatigue is displayed in every graph. It is characterized by a maximum value of  
333 500 HV measured 50  $\mu\text{m}$  below the surface and an estimated total hardened layer of about 600  $\mu\text{m}$ . These  
334 values are consistent with data from the literature on the 316L and 304L alloys after comparable surface  
335 mechanical attrition treatments [34, 40, 52, 53]. After cyclic loading for one cycle or more, the curves of the  
336 SMAT + Fat  $R_{TC}$ , SMAT + Fat  $R_{TT}$ , and SMAT + 1Cy  $R_{TT}$  samples depict a general gradient evolution that is  
337 quite similar to the reference SMAT one. However, when sufficient fatigue cycles were applied (i.e., for the  
338 two SMAT + Fat conditions in Figures 7 a and b), a slight softening was detected at the subsurface  
339 between 100 and 200  $\mu\text{m}$  (as indicated by the single red arrows), while, as pointed by the double red arrows  
340 below 600  $\mu\text{m}$ , a hardening was measured in the so-called “core material”. Differences in the behavior of  
341 dislocations can explain these two opposite phenomena. Indeed, during cyclic loading, the annihilation of

342 dislocations created under SMAT occurs, thus leading to softening in the subsurface. Similar explanation was  
 343 given in the work of Sun et al. in which a similar behavior was observed [33]. In the core material, new  
 344 dislocations were created during fatigue, and the material was hardened. The stabilized value in the core is  
 345 220 HV, which represents an increase of about 10 % compared to the initial hardness of the material. The  
 346 absence of significant differences for the SMAT + 1Cy  $R_{TT}$  sample indicates that several cycles of fatigue are  
 347 needed to reach the stabilized hardened state.

### 348 3.4. Crossland criterion

349 The fact that the residual stress gradient after fatigue was shown to be drastically different for both  
 350 loading conditions (RTC and RTT) indicates that not only the macroscopic loading has to be considered to  
 351 understand the influence of SMAT on the fatigue limits for those two load ratios. Moreover, as for each tested  
 352 conditions the fatigue limit was shown to be characterised by the incapacity of fatigue cracks to initiate, an  
 353 initiation endurance criterion taking into account the multiaxial stress field at the surface of the fatigue samples,  
 354 such as the Crossland criterion [54], seems to be a way to understand the difference of effectiveness of such  
 355 treatment in the HCF regime. Three hypotheses were considered to establish the Crossland criterion. The first  
 356 one is that the initial polished samples were exempt from residual stress due to the surface polishing after  
 357 machining. The second one is that the free surface of the SMAT samples is considered to be under a plane  
 358 stress state and that the shear components  $\sigma_{12}$  and  $\sigma_{21}$  are negligible compared to the longitudinal and tangential  
 359 ones  $\sigma_{11}$  and  $\sigma_{22}$ . The third one is that only the residual stress state measured in austenite was considered  
 360 because the proportion of martensite was limited and not quantified in detail, so that a “rule of mixtures” could  
 361 not be used. Considering that the estimated fatigue limits are  $\sigma_{RTC}^{\text{polished}} = 205$  MPa,  $\sigma_{RTC}^{\text{SMAT}} = 240$  MPa,  
 362  $\sigma_{RTT}^{\text{polished}} = 230$  MPa, and  $\sigma_{RTT}^{\text{SMAT}} = 215$  MPa, and that the stabilized surface residual stress tensors after fatigue  
 363 loading of the SMAT samples are:

$$364 \quad \underline{\underline{RS}}_{RTC}^{\text{SMAT}} \begin{bmatrix} -229 & \sim 0 & 0 \\ \sim 0 & -512 & 0 \\ 0 & 0 & 0 \end{bmatrix} \quad \text{and} \quad \underline{\underline{RS}}_{RTT}^{\text{SMAT}} \begin{bmatrix} +872 & \sim 0 & 0 \\ \sim 0 & -225 & 0 \\ 0 & 0 & 0 \end{bmatrix}$$

365 The following two stress tensors invariants were calculated.  $J_{1,\max} = \frac{1}{3} \text{tr}(\underline{\underline{\sigma}}_{\max})$  and  $\sqrt{J_{2,a}} = \sqrt{\frac{1}{2} \underline{\underline{S}}_a : \underline{\underline{S}}_a}$   
 366 where  $\underline{\underline{S}}_a$  is the stress amplitude tensor deviator defined by  $\underline{\underline{S}}_a = \underline{\underline{\sigma}}_a - \frac{1}{3} \text{tr}(\underline{\underline{\sigma}}_a) \cdot \underline{\underline{I}}$ . The results are plotted in  
 367 Figure 8 for the different load ratios and surface state conditions. The two points corresponding to the fatigue  
 368 limits of the polished conditions for  $R_{TC}$  (hollow circle) and  $R_{TT}$  (filled circle) are located in a similar  $\sqrt{J_{2,a}}$  area

369 of the graph due to the comparable measured fatigue limits. However, the point representing the polished  $R_{TT}$   
370 (filled circle) condition is shifted to the right on the  $J_{1,max}$  axis compared to the  $R_{TC}$  (hollow circle) one due to  
371 the higher maximum stress during cycle for this load ratio. Comparatively, for both SMAT conditions, the  
372 residual stress state acts as a mean stress during cyclic loading. Thus, due to the compressive stress field, the  
373 point corresponding to the  $R_{TC}$  SMAT condition (hollow square) is pushed in the region of the graph where  
374  $J_{1,max}$  is negative. Because of the surface tensile residual stresses for  $R_{TT}$  SMAT (filled square), the  
375 corresponding point is shifted to the right end side of the graph. The four points are almost aligned in a slightly  
376 decreasing trend indicating the negative effect of the maximum hydrostatic pressure, which is usually observed  
377 in the Crossland criterion representations [54, 55]. Moreover, the obtained fitted linear curve separates the  
378 graph into two regions. The region below the curve corresponds to the “safety domain” where failure will not  
379 occur. In contrast, the region above the line represents the “failure domain” in which cracking will occur, and  
380 fracture of the sample should happen.

#### 381 4. Discussions

382 The previous section has shown that the load ratio applied to a specimen has a non-negligible impact  
383 on the potential effect of SMAT on the HCF behavior of austenitic stainless steels. Indeed, our results have  
384 shown that the SMAT allowed to increase the fatigue limit of samples loaded at  $R_{TC} = -1$  by about +17 % for  
385 both the 316L and 304L steels, while a reduction of -7 % was observed when samples were loaded at  
386  $R_{TT} = +0.1$ . For  $R_{TC}$ , such improvement has already been observed in fully reversed loading ( $R = -1$ ), whether  
387 the steel was loaded in tension-compression [32, 40] or alternating flexural or rotating bending [18, 40]. In  
388 comparison, for  $R_{TT}$ , no direct comparison with data from the literature is available for stainless steels treated  
389 by SMAT. While mechanical surface treatments are carried out to enhance the fatigue limit of materials, they  
390 appear to potentially have the opposite effect and actually reduce it. In such case, it is most of the time attributed  
391 to the modified surface roughness and generated surface defects. Thus, the first section of this discussion will  
392 deal with the direct effect of the surface integrity on the fatigue behavior. This will be shown to be insufficient  
393 to fully explain the differences in behavior. Then, the influence of the plastic deformation mechanisms on the  
394 microstructure and hardness as well as the role of the residual stress evolutions and their effect on the fatigue  
395 crack initiation mechanisms will be discussed.

##### 396 4.1. Effect of the surface integrity on fatigue crack initiation

397 It is often proposed that the reduction in fatigue properties is due to surface defects that lead to faster  
398 fatigue crack initiation and compensate the benefits of the surface compressive residual stresses and hardened  
399 layer. This hypothesis can be found in several works focusing on a wide variety of materials and loading  
400 conditions. Kumar et al. studied uniaxial tension-tension fatigue at  $R = +0.1$  after 30 min and 60 min of SMAT  
401 on the 718 Inconel superalloy [56] and on a Ti-6Al-4V titanium alloy [24]. While minimal effect was obtained  
402 on the superalloy [56], the reduction of the fatigue limit observed after 60 min of SMAT in the Ti-alloy [24]  
403 was proposed to be due to the increase of micro-damage linked to the increased treatment time. Tian et al. drew  
404 a similar conclusion for a C-2000 nickel-based superalloy loaded at  $R = +0.1$  under four-point bending for  
405 which, after an improvement of 50 % in the fatigue limit after 30 min of SMAT, the fatigue life was  
406 systematically reduced when the treatment duration was increased (60 min, 90 min and 180 min). This was  
407 also discussed in the LCF and very high cycle fatigue (VHCF) regimes by Pandey et al. [57] and by  
408 Gao et al. [58], who respectively studied a 7075 aluminium alloy and a TC11 titanium alloy loaded at  $R = -1$   
409 after different SMAT-processing times. For the Al-alloy, the number of cycles to failure was almost unchanged  
410 after 30 sec and 60 sec of SMAT, increased for 180 sec but was reduced back to the initial performances after  
411 300 sec of surface modification treatment [57]. The number of cycles to failure of the Ti-alloy was reduced by  
412 approximately one to two decades for a “mild” surface modification condition and even further for a more  
413 drastic SMAT one [58]. These negative behaviours were again attributed to the easier initiation of the fatigue  
414 cracks which was cancelling the improved crack propagation resistance due to the compressive residual stress  
415 layer [57, 58]. Maurel et al. studied the effect of SMAT duration when combined with ageing heat treatment  
416 on the fatigue behavior of two aluminium alloys, namely a 2024 and 7075 series [26]. Some samples were aged  
417 before SMAT and some after SMAT. By carrying SMAT on the soft solution treated condition (SMAT before  
418 ageing), the fatigue limits were unchanged for the 2024 alloy and reduced by about 15 % for the 7075 one.  
419 Comparatively, for both materials, conducting SMAT on the hardened material (SMAT after ageing) led to a  
420 reduced samples surface roughness resulting in an increase of about 20 % of the fatigue limits.

421 Considering the non-negligible number of publications highlighting the fatigue life reduction after  
422 severe SMAT-processing as the consequence of the increased roughness, it would be tempting to attribute the  
423 reduction of the fatigue limit observed in this work at  $R_{TT}$  to the formation of dimples due to the high number  
424 of impacts. However, as shown in Figure 2, such initiation mechanism on dimples was only detected for the  
425 SMATed samples loaded at  $R_{TT}$  under low stress amplitudes. Instead, for the other  $R_{TT}$  conditions, crack  
426 initiation mainly occurred around inclusions that were already present in the raw material while no obvious



427 difference was found in the initiation sites comparing polished and SMATed samples for the  $R_{TC}$  conditions.  
428 However, it is clear that the “quality” of the surface has an effect on the fatigue properties. Indeed, for the  
429 SMAT samples that were mirror polished and tested at  $R_{TT}$ , the properties were restored to those of the initially  
430 polished material (Figure 1 b). Thus, the action of smoothing the surface after SMAT had a positive effect on  
431 the fatigue properties. From this point of view, Bagherifard et al. also observed an additional (+10 %) increase  
432 in the fatigue limit of severely shot peened low-alloy steel samples after conducting a grinding  
433 post-processing [59]. An additional confirmation of the importance of the surface state in initiating the fracture  
434 is the absence of any surface crack on the run-out samples (Figure 5). However, our overall results clearly  
435 show that, even if the roughness of the surface and the presence of stress raisers must have an effect on the  
436 fatigue properties, it is not the primary reason for the difference in behavior observed between the  $R_{TC}$  and  $R_{TT}$   
437 loading conditions.

#### 438 4.2. Effects of the cyclic stress on the plastic deformation mechanisms

439 Exploring alternative hypotheses for the variable effectiveness of SMAT to enhance the fatigue limit  
440 at  $R_{TC}$  and  $R_{TT}$ , the effect of the different type of loading has to be discussed. Indeed, the fact that half of the  
441 fatigue life of the samples tested at  $R_{TC}$  occurs under a compressive state and that the maximum stress during  
442 cycle is higher for  $R_{TT}$  imply very different macro- and micro- strains that may lead to the occurrence of  
443 different damage mechanisms. The difference in material response to the different loading conditions can be  
444 witnessed by two major observations. The first one is the self-heating of the samples observed at  $R_{TC}$  for a  
445 10 Hz frequency but not at  $R_{TT}$ . The self-heating at  $R_{TC}$  is not detailed in the present paper but is completely  
446 identical to the one observed on the 304L stainless steel studied in a previous work [40] in which the same  
447 fatigue behavior at  $R_{TC}$  was obtained (Figure 1 a). In contrast, no self-heating was recorded at  $R_{TT}$ . To observe  
448 such self-heating, a much higher loading frequency should probably be used. Indeed, Tian et al. also measured  
449 a self-heating on a 316LN loaded at  $R = -1$  at 10 Hz but had to increase the testing frequency to 70 Hz to start  
450 observing relevant self-heating at  $R = +0.1$  [60]. The second evidence is the difference in microstructure  
451 evolution in the core of the sample between the  $R_{TC}$  and  $R_{TT}$  loading conditions. Indeed, during the tension-  
452 compression cyclic loading of the SMATed samples, the martensitic transformation occurred at depth below  
453 200  $\mu\text{m}$  (Figure 6 a). Interestingly, this transformation did not occur in the regions closer to the surface at  
454 100-200  $\mu\text{m}$ , probably due to the too high density of dislocations already present in the SMATed highly  
455 hardened domain that prevented the austenite to martensite phase transformation. This is in good accordance  
456 with the literature about the conditions required for athermal martensitic transformation in steels. Indeed, it

457 was shown that enhancing the yield stress of the parent phase (austenite) by a moderate increase of the  
458 dislocation density [61, 62] or decreasing the grain size [63] both lead to a reduction in the  $M_S$  temperature.  
459 Such lowered value of  $M_S$  implies that a greater mechanical work is required to allow martensitic  
460 transformation; in other words, a greater stability of the austenite in this region. In contrast, neither stress- nor  
461 strain-assisted martensitic transformation was triggered under the tension-tension fatigue condition used in this  
462 work. Due to the negative values of  $M_S$  and  $M_{d30}$  for this alloy (Table 1), a significant strain is required to  
463 induce  $\gamma \rightarrow \alpha'$  phase transformation, as it was the case in the first 100  $\mu\text{m}$  due to the severe plastic deformation  
464 induced by SMAT. The fact that phase transformation occurred during cyclic loading under  $R_{TC}$  and not under  
465  $R_{TT}$  conditions seems rather counter intuitive. Indeed, it is widely admitted that the martensite volume increases  
466 with strain [61, 64] and such phenomena is considered in recent modelling [65]. Also, Lebedev et al. showed  
467 that for a 18Cr-10Ni stainless steel, the martensitic transformation is more advanced when the sample is  
468 subjected to tension than compression [66]. Then, considering that the samples are subjected to higher strains  
469 for  $R_{TT}$  than  $R_{TC}$  and are exclusively undergoing tensile loading at  $R_{TT}$ , it would be fair to expect a higher  
470 volume fraction of martensite for  $R_{TT}$  than  $R_{TC}$ . The exact opposite is observed here, indicating that other  
471 parameters are affecting the stability of austenite when subjected to cyclic loading. Lebedev et al. also reported  
472 that it is unusual to find martensite in fatigue loaded samples except on the crack path where the stress triaxiality  
473 is much higher than in the rest of the samples [66] which might be an essential aspect to consider in order to  
474 understand the observed phase transformation.

475 Nevertheless, even if these differences in the plastic deformation mechanisms and resulting  
476 microstructures were observed due to the different loading conditions, they are not at the origin of the  
477 differences in the fatigue properties. Indeed, the observed phase transformation is supposed to have negligible  
478 influence on the surface fatigue crack initiation because it occurred 200  $\mu\text{m}$  below the surface. In addition, in  
479 Figure 1 the 304L and the 316L stainless steels were shown to have identical fatigue behavior at  $R_{TC}$  even if  
480 Dureau et al. highlighted that the surface of the 304L was fully martensitic after SMAT [40]. Moreover, the  
481 analysis of hardness gradient after different fatigue loading conditions revealed limited changes in the  
482 hardening state in the SMAT affected region for  $R_{TC}$  and  $R_{TT}$  conditions. As the evolutions of hardness followed  
483 the same trends, it should have an equally beneficial contribution to the fatigue life enhancement for both load  
484 ratios after SMAT and, consequently, it is also not responsible for the fatigue life reduction at  $R_{TT}$ .

485 One of the major difference revealed by the analysis of the run-out samples is that the residual stress  
486 gradient evolutions after fatigue were drastically different under  $R_{TC}$  and  $R_{TT}$ . The compressive stress state

487 relaxation observed for  $R_{TC}$  was commonly observed after fatigue loading for many materials and testing  
488 conditions [4, 5, 19, 31, 40, 51] and sometimes even led to a fully relaxed stress field [34]. Comparatively, the  
489 gradient reversion leading to the formation of tensile residual stress gradient generally occurs for quasi-static  
490 loading or when overloads occur during fatigue [35, 67-71]. In our case, the inverted residual stress state was  
491 formed after the first cycle of fatigue and remained during the whole fatigue life of the samples. As the internal  
492 stresses redistributions are essentially a matter of mechanical equilibrium between the sub-surface layer  
493 affected by the SMAT and the core, the maximum applied stress during cyclic loading governs the residual  
494 stress evolutions. For the studied samples, the maximum applied loads during cycles were respectively  
495  $\sigma_{R_{TC} \max}^{SMAT} = 240$  MPa and  $\sigma_{R_{TT} \max}^{SMAT} = 477$  MPa.  $\sigma_{R_{TC} \max}^{SMAT}$  is then equal to 35% of the maximum tensile stress  
496  $\sigma_{UTS}$  (= 650 MPa), and 110 % of the yield stress  $\sigma_{ys}$  (= 220 MPa). On the other hand,  $\sigma_{R_{TT} \max}^{SMAT}$  is equal to 72%  
497 of  $\sigma_{UTS}$  thus 215 % of  $\sigma_{ys}$ . As  $\sigma_{R_{TC} \max}^{SMAT}$  was close to the yield stress, the core of the samples experienced small  
498 strains at  $R_{TC}$ , leading to moderate residual stress relaxations. In contrast,  $\sigma_{R_{TT} \max}^{SMAT}$  being twice the yield stress,  
499 the applied tensile strain has reverted the distribution of residual stresses. In both cases, those redistributed and  
500 stabilized residual stresses act as a local mean stress superimposed to the macroscopic loading, thus changing  
501 the stress field during cycling. This can help to understand the differences in the observed fatigue crack  
502 initiation mechanisms.

503 For the  $R_{TC}$  conditions, the maximum applied loads are just a few tens of MPa above the material  
504 elastic limit, causing only moderate and localized plastic strain. As confirmed by the surface analysis in  
505 Figure 2, these levels of plasticity are not large enough under the  $R_{TC}$  conditions to initiate cracking on  
506 inclusions regardless of the stress amplitude, especially for the SMAT samples due to the surface compressive  
507 residual stress. If Kakiuchi et al. observed one initiation on such calcium-aluminate inclusion in a 304L  
508 stainless steel treated by SMAT and then loaded at  $R = -1$  under rotating bending [72], it should be noticed that  
509 their fatigue tests were conducted at a temperature of 300 °C. It is possible that this elevated temperature can  
510 facilitate the use of these particles as stress raisers because it enhances the differences in mechanical properties  
511 between the austenitic matrix and the hard inclusion.

512 For the  $R_{TT}$  conditions, the much higher applied stress than for  $R_{TC}$  led to macroscopic straining of the  
513 samples highlighted by the high density of slip bands in Figure 2, thus damaging the inclusions interface with  
514 the steel matrix. This allowed the inclusions to be activated as initiation sites. This is particularly true for the

515 SMATed and SMAT + polished samples due to the superimposed macroscopic tensile loading and surface high  
516 tensile residual stress states.

517 Finally, as the surface inspection of the run-out samples never revealed non-propagating fatigue  
518 cracks, the resistance of the material to fatigue crack initiation was shown to rule the fatigue limit in the high  
519 cycle fatigue regime. Then, the redistributed residual stress fields were taken into account into a Crossland  
520 fatigue initiation criterion and provided a good description of both the effect of load ratio and SMAT. The  
521 residual stress state was then considered the first-order parameter governing the fatigue performance of  
522 SMATed austenitic stainless steels samples. Therefore, the development of numerical models to predict the  
523 cyclic response of SMATed samples and the residual stress field evolutions after such cyclic loading seems to  
524 be a very interesting way of predicting the fatigue life of gradient microstructure stainless steels components  
525 under various loading conditions.

## 526 **6. Conclusions**

527 Uniaxial fatigue tests have been conducted on an austenitic stainless steel with load ratios  $R_{TC} = -1$  and  
528  $R_{TT} = +0.1$ , to evaluate the high cycle fatigue performance of the gradient microstructure generated by SMAT  
529 in a context of local or general plasticity. The fatigue limit change resulting from SMAT was beneficial  
530 at  $R_{TC} = -1$  (+17 %) and detrimental at  $R_{TT} = +0.1$  (-7 %).

531 After fatigue loading, no cracks were detected at the surface of any of the run-out samples, indicating that the  
532 resistance to fatigue crack initiation was governing the fatigue limit in the HCF regime. Processing inclusions  
533 already present in the initial material were the predominant initiation sites for crack nucleation for  $R_{TT}$  rather  
534 than surface defects. The evolution of residual stresses was proved to be the primary parameter governing the  
535 fatigue response: the compressive residual stress generated by SMAT was partially relaxed at  $R_{TC}$  while it was  
536 fully reverted after only one cycle of  $R_{TT}$  loading.

537 The beneficial effect on the fatigue limit (improved by +17 %) for  $R_{TC} = -1$  loading is due to the sub-surface  
538 compressive residual stresses present in the hardened gradient microstructure that overcome the negative effect  
539 of the surface defects induced by SMAT. During fatigue loading at  $R_{TC}$ , self-heating of all the specimens  
540 occurred together with sub-surface martensitic transformation for the SMATed samples. Nevertheless, these  
541 two modifications had a negligible impact on the fatigue properties.

542 The detrimental effect on the fatigue limit (reduced by -7 %) for  $R_{TT} = +0.1$  is associated to the high imposed  
543 macroscopic stresses that caused a complete reversion of the compressive residual stress gradient towards  
544 tension. This very high tensile stress leads to faster fatigue crack initiation compared to the untreated material.  
545 In this case, no self-heating nor sub-surface martensitic transformation were revealed, but the much higher  
546 stress at  $R_{TT}$  was proposed to be responsible for the initiations on inclusions. In this case, the combined negative  
547 effects of tensile residual stresses and surface roughness leads to a slightly reduced fatigue limit for SMAT  
548 specimens.

549 For the  $R_{TT}$  loading condition, a mirror polishing procedure after SMAT allowed to restore the fatigue limit  
550 (same as the untreated condition) but did not improve it. This is a confirmation that (i) the redistribution of  
551 residual stress was of primary importance for controlling the high cycle fatigue behavior and (ii) the surface  
552 defects created by SMAT were not responsible for the incapacity of the SMAT to improve the fatigue limit at  
553  $R_{TT}$ .

554

### 555 **Acknowledgement**

556 This work was supported by the French State through the program “Investment in the future” operated by the  
557 National Research Agency (ANR), referenced by ANR-11-LABX-0008-01 (Labex DAMAS).

558 This work was also supported by the CPER FEDER project of Région Nouvelle Aquitaine.

### 559 **Declaration of competing interest**

560 The authors declare that they have no known competing financial interests or personal relationships that could  
561 have appeared to influence the work reported in this paper.

### 562 **References**

563 [1] Y. Miyamoto, W.A. Kaysser, B.H. Rabin, A. Kawasaki, R.G. Ford, Functionally Graded Materials:  
564 Design, Processing and Applications, Kluwer Academic Publishers, Hingham, MA (US), United States,  
565 (1999). <https://doi.org/10.1007/978-1-4615-5301-4>

566 [2] B. Kieback, A. Neubrand, H. Riedel, Processing techniques for functionally graded materials,  
567 Materials Science and Engineering: A, 362(1-2) (2003) 81-106. DOI: [https://doi.org/10.1016/S0921-](https://doi.org/10.1016/S0921-5093(03)00578-1)  
568 5093(03)00578-1

- 569 [3] K. Dalaei, B. Karlsson, Influence of shot peening on fatigue durability of normalized steel subjected  
570 to variable amplitude loading, *International journal of fatigue*, 38 (2012) 75-83.  
571 DOI: <https://doi.org/10.1016/j.ijfatigue.2011.11.011>
- 572 [4] J.C. Kim, S.K. Cheong, H. Noguchi, Residual stress relaxation and low-and high-cycle fatigue  
573 behavior of shot-peened medium-carbon steel, *International Journal of Fatigue*, 56 (2013) 114-122.  
574 DOI: <https://doi.org/10.1016/j.ijfatigue.2013.07.001>
- 575 [5] M. Benedetti, V. Fontanari, C. Santus, M. Bandini, Notch fatigue behavior of shot peened high-  
576 strength aluminium alloys: Experiments and predictions using a critical distance method, *International Journal*  
577 *of Fatigue*, 32(10) (2010) 1600-1611. DOI: <https://doi.org/10.1016/j.ijfatigue.2010.02.012>
- 578 [6] H. Luong, M.R. Hill, The effects of laser peening and shot peening on high cycle fatigue in 7050-  
579 T7451 aluminum alloy, *Materials Science and Engineering: A*, 527(3) (2010) 699-707.  
580 DOI: <https://doi.org/10.1016/j.msea.2009.08.045>
- 581 [7] M. Benedetti, T. Bortolamedi, V. Fontanari, F. Frendo, Bending fatigue behavior of differently shot  
582 peened Al 6082 T5 alloy, *International journal of fatigue*, 26(8) (2004) 889-897.  
583 DOI: <https://doi.org/10.1016/j.ijfatigue.2003.12.003>
- 584 [8] S. Bagheri, M. Guagliano, Review of shot peening processes to obtain nanocrystalline surfaces in  
585 metal alloys, *Surface Engineering*, 25(1) (2009) 3-14. DOI: <https://doi.org/10.1179/026708408X334087>
- 586 [9] J. Azadmanjiri, C.C. Berndt, A. Kapoor, C. Wen, Development of surface nano-crystallization in  
587 alloys by surface mechanical attrition treatment (SMAT), *Critical Reviews in Solid State and Materials*  
588 *Sciences*, 40(3) (2015) 164-181. DOI: <https://doi.org/10.1080/10408436.2014.978446>
- 589 [10] T. Grosdidier, M. Novelli, Recent developments in the application of surface mechanical attrition  
590 treatments for improved gradient structures: processing parameters and surface reactivity. *Materials*  
591 *transactions*, 60(7) (2019) 1344-1355. DOI: <https://doi.org/10.2320/matertrans.MF201929>
- 592 [11] D. Kumar, S. Idapalapati, W. Wang, S. Narasimalu, Effect of surface mechanical treatments on the  
593 microstructure-property-performance of engineering alloys, *Materials*, 12(16) (2019) 2503.  
594 DOI: <https://doi.org/10.3390/ma12162503>

- 595 [12] T.O. Olugbade, J. Lu, Literature review on the mechanical properties of materials after surface  
596 mechanical attrition treatment (SMAT), *Nano Materials Science*, 2(1) (2020) 3-31.  
597 DOI: <https://doi.org/10.1016/j.nanoms.2020.04.002>
- 598 [13] Y. Samih, B. Beausir, B. Bolle, T. Grosdidier, In-depth quantitative analysis of the microstructures  
599 produced by Surface Mechanical Attrition Treatment (SMAT), *Materials characterization*, 83 (2013) 129-138.  
600 DOI: <https://doi.org/10.1016/j.matchar.2013.06.006>
- 601 [14] G. Proust, D. Retraint, M. Chemkhi, A. Roos, C. Demangel, Electron backscatter diffraction and  
602 transmission Kikuchi diffraction analysis of an austenitic stainless steel subjected to surface mechanical  
603 attrition treatment and plasma nitriding, *Microscopy and Microanalysis*, 21(4) (2015) 919-926.  
604 DOI: <https://doi.org/10.1017/S1431927615000793>
- 605 [15] C. Xin, D. Yang, Q. Sun, L. Xiao, J. Sun, Thermal stability of nanogradient microstructure produced  
606 by surface mechanical rolling treatment in Zircaloy-4, *Journal of Materials Science*, 55(11) (2020) 4926-4939.  
607 DOI: <https://doi.org/10.1007/s10853-019-04303-z>
- 608 [16] K. Skowron, E. Dryzek, M. Wróbel, P. Nowak, M. Marciszko-Wiąckowska, L. Le Joncour, M.  
609 François, B. Panicaud, A. Baczmański, Gradient Microstructure Induced by Surface Mechanical Attrition  
610 Treatment (SMAT) in Magnesium Studied Using Positron Annihilation Spectroscopy and Complementary  
611 Methods, *Materials*, 13(18) (2020) 4002. DOI: <https://doi.org/10.3390/ma13184002>
- 612 [17] J.C. Villegas, L.L. Shaw, K. Dai, W. Yuan, J. Tian, P.K. Liaw, D.L. Klarstrom, Enhanced fatigue  
613 resistance of a nickel-based hastelloy induced by a surface nanocrystallization and hardening process,  
614 *Philosophical magazine letters*, 85(8) (2005) 427-438. DOI: <https://doi.org/10.1080/09500830500311705>
- 615 [18] J. Uusitalo, L.P. Karjalainen, D. Retraint, M. Palosaari, Fatigue properties of steels with ultrasonic  
616 attrition treated surface layers, In: *Materials science forum*, Trans Tech Publications Ltd., Vol. 604 (2009)  
617 239-248. DOI: <https://doi.org/10.4028/www.scientific.net/MSF.604-605.239>
- 618 [19] L.L. Shaw, J.W. Tian, A.L. Ortiz, K. Dai, J.C. Villegas, P.K. Liaw, R. Ren, D.L. Klarstrom, A direct  
619 comparison in the fatigue resistance enhanced by surface severe plastic deformation and shot peening in a C-  
620 2000 superalloy, *Materials Science and Engineering: A*, 527(4-5) (2010) 986-994.  
621 DOI: <https://doi.org/10.1016/j.msea.2009.10.028>

- 622 [20] L. Yang, N.R. Tao, K. Lu, L. Lu, Enhanced fatigue resistance of Cu with a gradient nanograined  
623 surface layer, *Scripta Materialia*, 68(10) (2013) 801-804.  
624 DOI: <https://doi.org/10.1016/j.scriptamat.2013.01.031>
- 625 [21] M.K. Khan, M.E. Fitzpatrick, Q.Y. Wang, Y.S. Pyoun, A. Amanov, Effect of ultrasonic nanocrystal  
626 surface modification on residual stress and fatigue cracking in engineering alloys, *Fatigue & Fracture of  
627 Engineering Materials & Structures*, 41(4) (2018) 844-855. DOI: <https://doi.org/10.1111/ffe.12732>
- 628 [22] S. Bagherifard, I. Fernandez-Pariente, R. Ghelichi, M. Guagliano, Effect of severe shot peening on  
629 microstructure and fatigue strength of cast iron, *International Journal of Fatigue*, 65 (2014) 64-70.  
630 DOI: <https://doi.org/10.1016/j.ijfatigue.2013.08.022>
- 631 [23] J.W. Tian, J.C. Villegas, W. Yuan, D. Fielden, L. Shaw, P.K. Liaw, D.L. Klarstrom, A study of the  
632 effect of nanostructured surface layers on the fatigue behaviors of a C-2000 superalloy, *Materials Science and  
633 Engineering: A*, 468 (2007) 164-170. DOI: <https://doi.org/10.1016/j.msea.2006.10.150>
- 634 [24] S.A. Kumar, S.G.S. Raman, T.S. Narayanan, Influence of surface mechanical attrition treatment  
635 duration on fatigue lives of Ti-6Al-4V, *Transactions of the Indian Institute of Metals*, 67(1) (2014) 137-141.  
636 DOI: <https://doi.org/10.1007/s12666-013-0322-2>
- 637 [25] Y. Feng, S. Hu, D. Wang, L. Cui, Formation of short crack and its effect on fatigue properties of  
638 ultrasonic peening treatment S355 steel, *Materials & Design*, 89 (2016) 507-515.  
639 DOI: <https://doi.org/10.1016/j.matdes.2015.10.009>
- 640 [26] P. Maurel, L. Weiss, T. Grosdidier, P. Bocher, How does surface integrity of nanostructured surfaces  
641 induced by severe plastic deformation influence fatigue behaviors of Al alloys with enhanced  
642 precipitation?, *International Journal of Fatigue*, 140 (2020) 105792.  
643 DOI: <https://doi.org/10.1016/j.ijfatigue.2020.105792>
- 644 [27] P. Maurel, L. Weiss, P. Bocher, T. Grosdidier, Effects of SMAT at cryogenic and room temperatures  
645 on the kink band and martensite formations with associated fatigue resistance in a  $\beta$ -metastable titanium  
646 alloy, *Materials Science and Engineering: A*, 803 (2021) 140618.  
647 DOI: <https://doi.org/10.1016/j.msea.2020.140618>



- 648 [28] F.K. Yan, G.Z. Liu, N.R. Tao, K. Lu, Strength and ductility of 316L austenitic stainless steel  
649 strengthened by nano-scale twin bundles, *Acta Materialia*, 60(3) (2012) 1059-1071.  
650 DOI: <https://doi.org/10.1016/j.actamat.2011.11.009>
- 651 [29] J. Li, Y. Cao, B. Gao, Y. Li, Y. Zhu, Superior strength and ductility of 316L stainless steel with  
652 heterogeneous lamella structure, *Journal of Materials Science*, 53(14) (2018) 10442-10456.  
653 DOI: <https://doi.org/10.1007/s10853-018-2322-4>
- 654 [30] H. Ueno, K. Kakihata, Y. Kaneko, S. Hashimoto, A. Vinogradov, Enhanced fatigue properties of  
655 nanostructured austenitic SUS 316L stainless steel, *Acta Materialia*, 59(18) (2011) 7060-7069.  
656 DOI: <https://doi.org/10.1016/j.actamat.2011.07.061>
- 657 [31] K. Masaki, Y. Ochi, T. Matsumura, Initiation and propagation behavior of fatigue cracks in hard-shot  
658 peened Type 316L steel in high cycle fatigue, *Fatigue & Fracture of Engineering Materials & Structures*, 27(12)  
659 (2004) 1137-1145. DOI: <https://doi.org/10.1111/j.1460-2695.2004.00824.x>
- 660 [32] T. Roland, D. Reirant, K. Lu, J. Lu, Fatigue life improvement through surface nanostructuring of  
661 stainless steel by means of surface mechanical attrition treatment, *Scripta Materialia*, 54(11) (2006) 1949-1954.  
662 DOI: <https://doi.org/10.1016/j.scriptamat.2006.01.049>
- 663 [33] Z. Sun, M. Chemkhi, P. Kanoute, D. Reirant, Fatigue properties of a biomedical 316L steel processed  
664 by surface mechanical attrition, In: *IOP Conference Series: Materials Science and Engineering*, 63 (2014)  
665 012021. DOI: <https://doi.org/10.1088/1757-899x/63/1/012021>
- 666 [34] Z. Sun, J. Zhou, D. Reirant, T. Baudin, A.L. Helbert, F. Brisset, P. Kanouté, Low cycle fatigue of  
667 316L stainless steel processed by surface mechanical attrition treatment (SMAT), In: *MATEC Web of  
668 Conferences*, EDP Sciences, 165 (2018) 15002. DOI: <https://doi.org/10.1051/mateconf/201816515002>
- 669 [35] H.W. Huang, Z.B. Wang, J. Lu, K. Lu, Fatigue behaviors of AISI 316L stainless steel with a gradient  
670 nanostructured surface layer, *Acta Materialia*, 87 (2015) 150-160.  
671 DOI: <https://doi.org/10.1016/j.actamat.2014.12.057>
- 672 [36] SONATS company website available online: <https://sonats-et.com/> (accessed on 27 October 2021).
- 673 [37] B. Beausir, J.-J. Fundenberger, Analysis Tools for Electron and X-ray diffraction, ATEX - software,  
674 [www.atex-software.eu](http://www.atex-software.eu), Université de Lorraine - Metz, (2017).

- 675 [38] M. G. Moore, W. P. Evans, Mathematical correction for stress in removed layers in X-ray diffraction  
676 residual stress analysis. SAE transactions, (1958) 340-345. DOI: <https://doi.org/10.4271/580035>
- 677 [39] C.E. Stromeyer, The determination of fatigue limits under alternating stress conditions. Proceedings  
678 of the Royal Society of London, Series A, Containing Papers of a Mathematical and Physical Character,  
679 90(620) (1914) 411-425. DOI: <https://doi.org/10.1098/rspa.1914.0066>
- 680 [40] C. Dureau, M. Novelli, M. Arzaghi, R. Massion, P. Bocher, Y. Nadot, T. Grosdidier, On the influence  
681 of ultrasonic surface mechanical attrition treatment (SMAT) on the fatigue behavior of the 304L austenitic  
682 stainless steel, *Metals*, 10(1) (2020) 100. DOI: <https://doi.org/10.3390/met10010100>
- 683 [41] L. Zhang, B.G. Thomas, Inclusions in continuous casting of steel, In: XXIV National Steelmaking  
684 Symposium, Morelia, Mexico, 26 (2003) 28.
- 685 [42] Y. Samih, M. Novelli, T. Thiriet, B. Bolle, N. Allain, J.-J. Funderberger, G. Marcos, T. Czerwicz, T.  
686 Grosdidier, Plastic deformation to enhance plasma-assisted nitriding: On surface contamination induced by  
687 Surface Mechanical Attrition Treatment, In: IOP Conference Series: Materials Science and Engineering, 63  
688 (2014) 012020. DOI: <https://doi.org/10.1088/1757-899x/63/1/012020>
- 689 [43] M. Chemkhi, D. Reirant, A. Roos, C. Demangel, Role and effect of mechanical polishing on the  
690 enhancement of the duplex mechanical attrition/plasma nitriding treatment of AISI 316L steel, *Surface and*  
691 *Coatings Technology*, 325 (2017) 454-461. DOI: <https://doi.org/10.1016/j.surfcoat.2017.06.052>
- 692 [44] P. Maurel, L. Weiss, P. Bocher, E. Fleury, T. Grosdidier, Oxide dependent wear mechanisms of  
693 titanium against a steel counterface: Influence of SMAT nanostructured surface, *Wear*, 430 (2019) 245-255.  
694 DOI: <https://doi.org/10.1016/j.wear.2019.05.007>
- 695 [45] T. Niendorf, F. Rubitschek, H.J. Maier, D. Canadinc, I. Karaman, On the fatigue crack growth–  
696 microstructure relationship in ultrafine-grained interstitial-free steel, *Journal of materials science*, 45(17)  
697 (2010) 4813-4821. DOI: <https://doi.org/10.1007/s10853-010-4511-7>
- 698 [46] K. Hockauf, M. Hockauf, M.X. Wagner, T. Lampke, T. Halle, Fatigue crack propagation in an ECAP-  
699 processed aluminium alloy–influence of shear plane orientation, *Materialwissenschaft und*  
700 *Werkstofftechnik*, 43(7) (2012) 609-616. DOI: <http://dx.doi.org/10.1002/mawe.201200008>

701 [47] M. Arzaghi, C. Sarrazin-Baudoux, J. Petit, Fatigue crack growth in ultrafine-grained copper obtained  
702 by ECAP, In: *Advanced Materials Research*, Trans Tech Publications Ltd., 891 (2014) 1099-1104.  
703 DOI: <https://doi.org/10.4028/www.scientific.net/AMR.891-892.1099>

704 [48] R. Blonde, H.L. Chan, N. Allain-Bonasso, B. Bolle, T. Grosdidier, J. Lu, Evolution of texture and  
705 microstructure in pulsed electro-deposited Cu treated by Surface Mechanical Attrition Treatment  
706 (SMAT), *Journal of Alloys and Compounds*, 504 (2010) S410-S413.  
707 DOI: <https://doi.org/10.1016/j.jallcom.2010.04.040>

708 [49] B. Cotterell, J. Rice, Slightly curved or kinked cracks, *International journal of fracture*, 16(2) (1980)  
709 155-169. DOI: <https://doi.org/10.1007/BF00012619>

710 [50] M. Novelli, P. Bocher, T. Grosdidier, Effect of cryogenic temperatures and processing parameters on  
711 gradient-structure of a stainless steel treated by ultrasonic surface mechanical attrition treatment, *Materials*  
712 *Characterization*, 139 (2018) 197-207. DOI: <https://doi.org/10.1016/j.matchar.2018.02.028>

713 [51] Y.B. Lei, Z.B. Wang, J.L. Xu, K. Lu, Simultaneous enhancement of stress-and strain-controlled  
714 fatigue properties in 316L stainless steel with gradient nanostructure, *Acta Materialia*, 168 (2019) 133-142.  
715 DOI: <https://doi.org/10.1016/j.actamat.2019.02.008>

716 [52] F. Yin, S. Hu, R. Xu, X. Han, D. Qian, W. Wei, L. Hua, K. Zhao, Strain rate sensitivity of the  
717 ultrastrong gradient nanocrystalline 316L stainless steel and its rate-dependent modeling at  
718 nanoscale, *International Journal of Plasticity*, 129 (2020) 102696.  
719 DOI: <https://doi.org/10.1016/j.ijplas.2020.102696>

720 [53] M. Novelli, J.-J. Fundenberger, P. Bocher, T. Grosdidier, On the effectiveness of surface severe plastic  
721 deformation by shot peening at cryogenic temperature, *Applied Surface Science*, 389 (2016) 1169-1174.  
722 DOI: <https://doi.org/10.1016/j.apsusc.2016.08.009>

723 [54] B. Crossland, Effect of large hydrostatic pressures on the torsional fatigue strength of an alloy steel,  
724 In: *Proceedings of the International Conference on Fatigue of Metals*, Institution of Mechanical Engineers  
725 London, 138 (1956) 12-12.

726 [55] P. Mu, Y. Nadot, C. Nadot-Martin, A. Chabod, I. Serrano-Munoz, C. Verdu, Influence of casting  
727 defects on the fatigue behavior of cast aluminum AS7G06-T6, *International Journal of Fatigue*, 63 (2014) 97-  
728 109. DOI: <https://doi.org/10.1016/j.ijfatigue.2014.01.011>

- 729 [56] S.A. Kumar, S.G.S. Raman, T.S. Narayanan, Effect of surface mechanical attrition treatment on  
730 fatigue lives of alloy 718, *Transactions of the Indian Institute of Metals*, 65(5) (2012) 473-477.  
731 DOI: <https://doi.org/10.1007/s12666-012-0154-5>
- 732 [57] V. Pandey, K. Chattopadhyay, N.S. Srinivas, V. Singh, Role of ultrasonic shot peening on low cycle  
733 fatigue behavior of 7075 aluminium alloy, *International Journal of Fatigue*, 103 (2017) 426-435.  
734 DOI: <https://doi.org/10.1016/j.ijfatigue.2017.06.033>
- 735 [58] T. Gao, Z. Sun, H. Xue, D. Reirant, Effect of Surface Mechanical Attrition Treatment on the very  
736 high cycle fatigue behavior of TC11, In: *MATEC Web of Conferences*, EDP Sciences, 165 (2018) 09001.  
737 DOI: <https://doi.org/10.1051/mateconf/201816509001>
- 738 [59] S. Bagherifard, M. Guagliano, Fatigue behavior of a low-alloy steel with nanostructured surface  
739 obtained by severe shot peening, *Engineering Fracture Mechanics*, 81 (2012) 56-68.  
740 DOI: <https://doi.org/10.1016/j.engfracmech.2011.06.011>
- 741 [60] H. Tian, P.K. Liaw, D.E. Fielden, C.R. Brooks, M.D. Brotherton, L. Jiang, B. Yang, H. Wang, J.P.  
742 Strizak, L.K. Mansur, Effects of frequency on fatigue behavior of type 316 low-carbon, nitrogen-added  
743 stainless steel in air and mercury for the spallation neutron source, *Metallurgical and materials transactions A*,  
744 37(1) (2006) 163-173. DOI: <https://doi.org/10.1007/s11661-006-0161-4>
- 745 [61] G.B. Olson, M. Cohen, Kinetics of strain-induced martensitic nucleation, *Metallurgical transactions*  
746 *A*, 6(4) (1975) 791. DOI: <https://doi.org/10.1007/BF02672301>
- 747 [62] M. Tokizane, The effect of tensile pre-straining on nucleation of martensite in an Fe-Ni-C  
748 alloy, *Scripta Metallurgica*, 10(5) (1976) 459-462. DOI: [https://doi.org/10.1016/0036-9748\(76\)90173-3](https://doi.org/10.1016/0036-9748(76)90173-3)
- 749 [63] S. Kajiwara, Roles of dislocations and grain boundaries in martensite nucleation, *Metallurgical and*  
750 *Materials Transactions A*, 17(10) (1986) 1693-1702. DOI: <https://doi.org/10.1007/BF02817268>
- 751 [64] D. Hennessy, G. Steckel, C. Altstetter, Phase transformation of stainless steel during  
752 fatigue, *Metallurgical Transactions A*, 7(3) (1976) 415-424. DOI: <https://doi.org/10.1007/BF02642838>
- 753 [65] E.I. Galindo-Nava, P.E.J. Rivera-Díaz-del-Castillo, Understanding martensite and twin formation in  
754 austenitic steels: A model describing TRIP and TWIP effects, *Acta Materialia*, 128 (2017) 120-134.  
755 DOI: <https://doi.org/10.1016/j.actamat.2017.02.004>

- 756 [66] A.A. Lebedev, V.V. Kosarchuk, Influence of phase transformations on the mechanical properties of  
757 austenitic stainless steels, *International Journal of Plasticity*, 16(7-8) (2000) 749-767.  
758 DOI: [https://doi.org/10.1016/S0749-6419\(99\)00085-6](https://doi.org/10.1016/S0749-6419(99)00085-6)
- 759 [67] A. Wick, V. Schulze, O. Vöhringer, Effects of warm peening on fatigue life and relaxation behavior  
760 of residual stresses in AISI 4140 steel, *Materials Science and Engineering: A*, 293(1-2) (2000) 191-197.  
761 DOI: [https://doi.org/10.1016/S0921-5093\(00\)01035-2](https://doi.org/10.1016/S0921-5093(00)01035-2)
- 762 [68] K. Dalaei, B. Karlsson, L.E. Svensson, Stability of shot peening induced residual stresses and their  
763 influence on fatigue lifetime, *Materials Science and Engineering: A*, 528(3) (2011) 1008-1015.  
764 DOI: <https://doi.org/10.1016/j.msea.2010.09.050>
- 765 [69] W.Z. Zhuang, G.R. Halford Investigation of residual stress relaxation under cyclic load, *International*  
766 *journal of fatigue*, 23 (2001) 31-37. DOI: [https://doi.org/10.1016/S0142-1123\(01\)00132-3](https://doi.org/10.1016/S0142-1123(01)00132-3)
- 767 [70] K. Dalaei, B. Karlsson, Influence of overloading on fatigue durability and stability of residual stresses  
768 in shot peened normalized steel, *Materials Science and Engineering: A*, 528(24) (2011) 7323-7330.  
769 DOI: <https://doi.org/10.1016/j.msea.2011.06.002>
- 770 [71] D.J. Buchanan, R. John, Residual stress redistribution in shot peened samples subject to mechanical  
771 loading, *Materials Science and Engineering: A*, 615 (2014) 70-78.  
772 DOI: <https://doi.org/10.1016/j.msea.2014.06.118>
- 773 [72] T. Kakiuchi, Y. Uematsu, N. Hasegawa, E. Kondoh, Effect of ultrasonic shot peening on high cycle  
774 fatigue behavior in type 304 stainless steel at elevated temperature, *J. Soc. Mater. Sci.* 65 (2016) 325–330.  
775 DOI: <https://doi.org/10.2472/jsms.65.325>

776

*Table 1 Chemical composition of the studied 316L stainless steel*

	C	Mn	Si	S	P	Cr	Ni	Mo	Cu	N	Fe	$M_S$ [° C]	$M_{d30}$ [° C]
Wt [%]	0.029	1.499	0.341	0.03	0.22	16.605	10.370	2.036	0.127	0.047	Balance	-210	-1

777

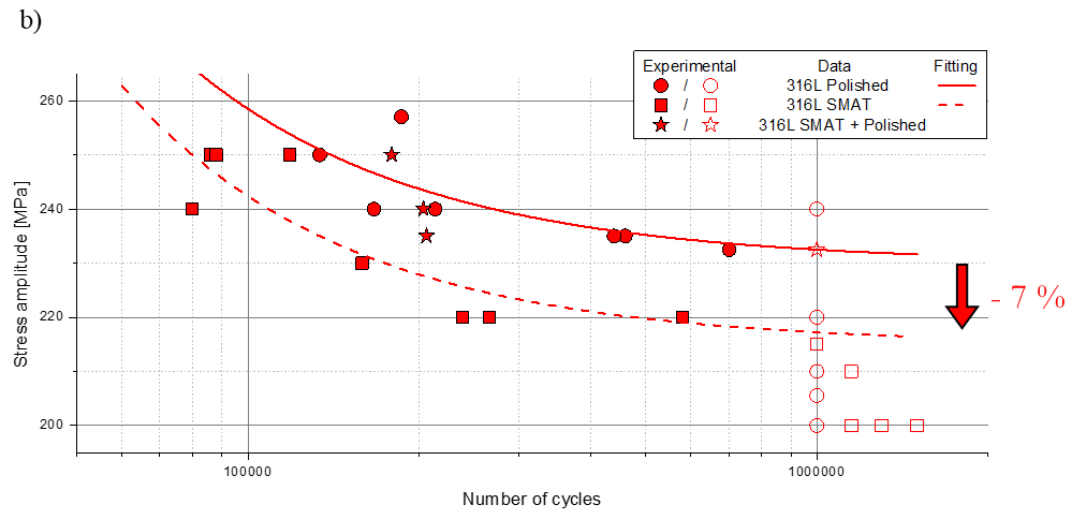
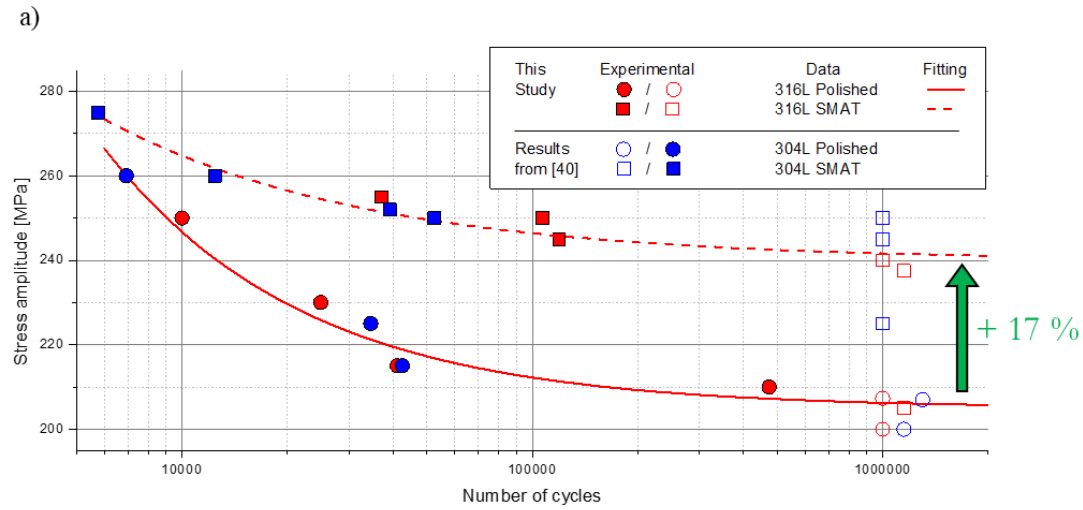
Table 2 Different a) fatigue testing conditions and b) analysed unbroken samples

a)

Testing condition name	Step 1	Step 2	Step 3	Step 4	Step 5	Ra [ $\mu\text{m}$ ]
Initially polished	Heat treated 900 °C 40 min	Machined	Mirror polished	/	/	$0.017 \pm 2.5 \cdot 10^{-3}$
SMAT				SMATed	/	$1.621 \pm 0.23$
SMAT + polished					Mirror polished	$0.018 \pm 1.4 \cdot 10^{-3}$

b)

Analysed unbroken sample	Load ratio	Stress amplitude [MPa]	Number of cycles
SMAT	/	/	/
SMAT + Fat $R_{TC}$	-1	240	$2 \cdot 10^6$
SMAT + Fat $R_{TT}$	+0.1	215	$4 \cdot 10^6$
SMAT + 1Cy $R_{TT}$	+0.1	215	1



779

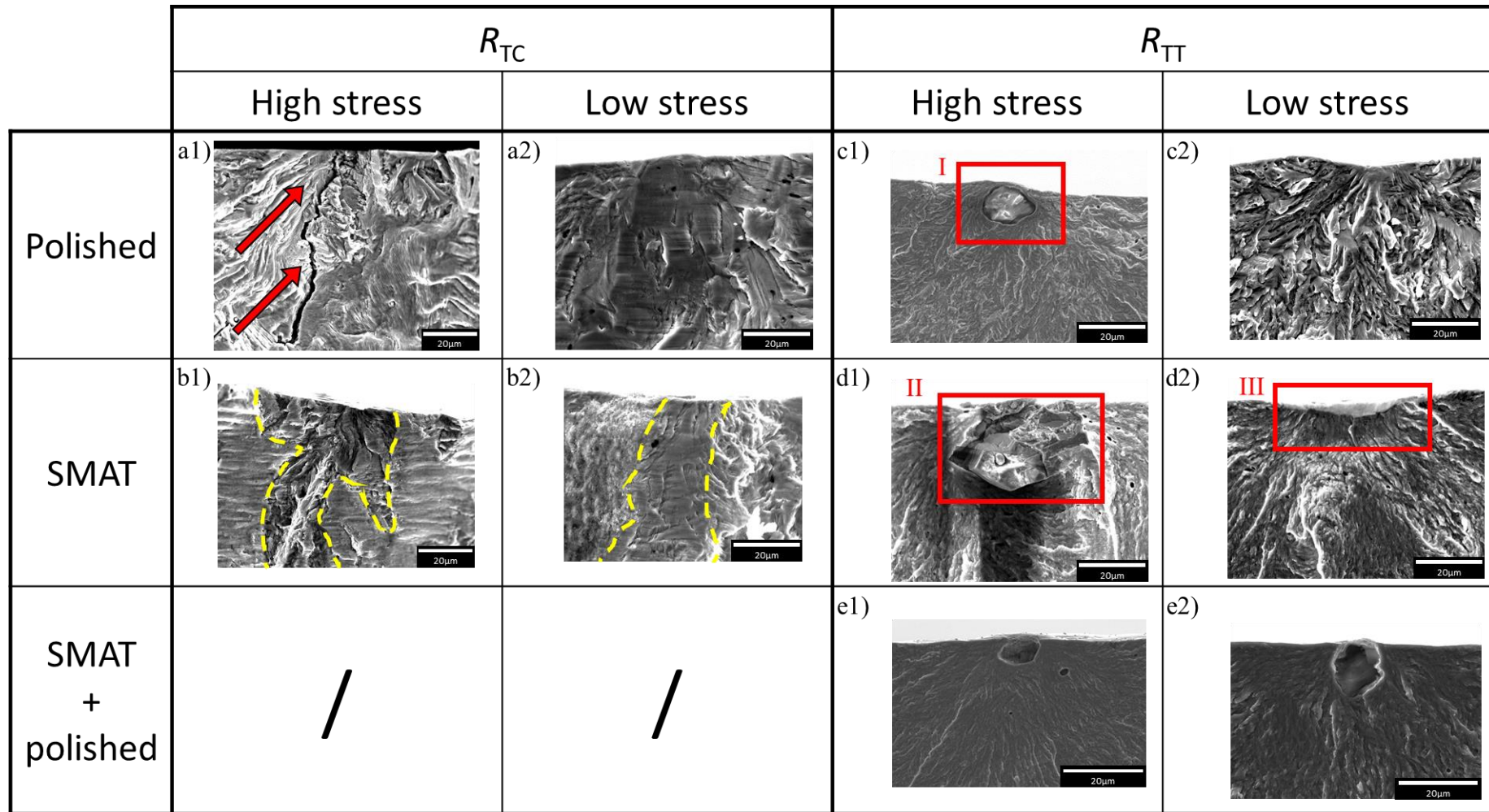
780

Figure 1 Wöhler curves of a) polished and SMAT 316L and 304L samples loaded at  $R_{TC}=-1$  and b) polished, SMAT and SMAT + polished 316L samples loaded at

781

$R_{TT}=+0.1$



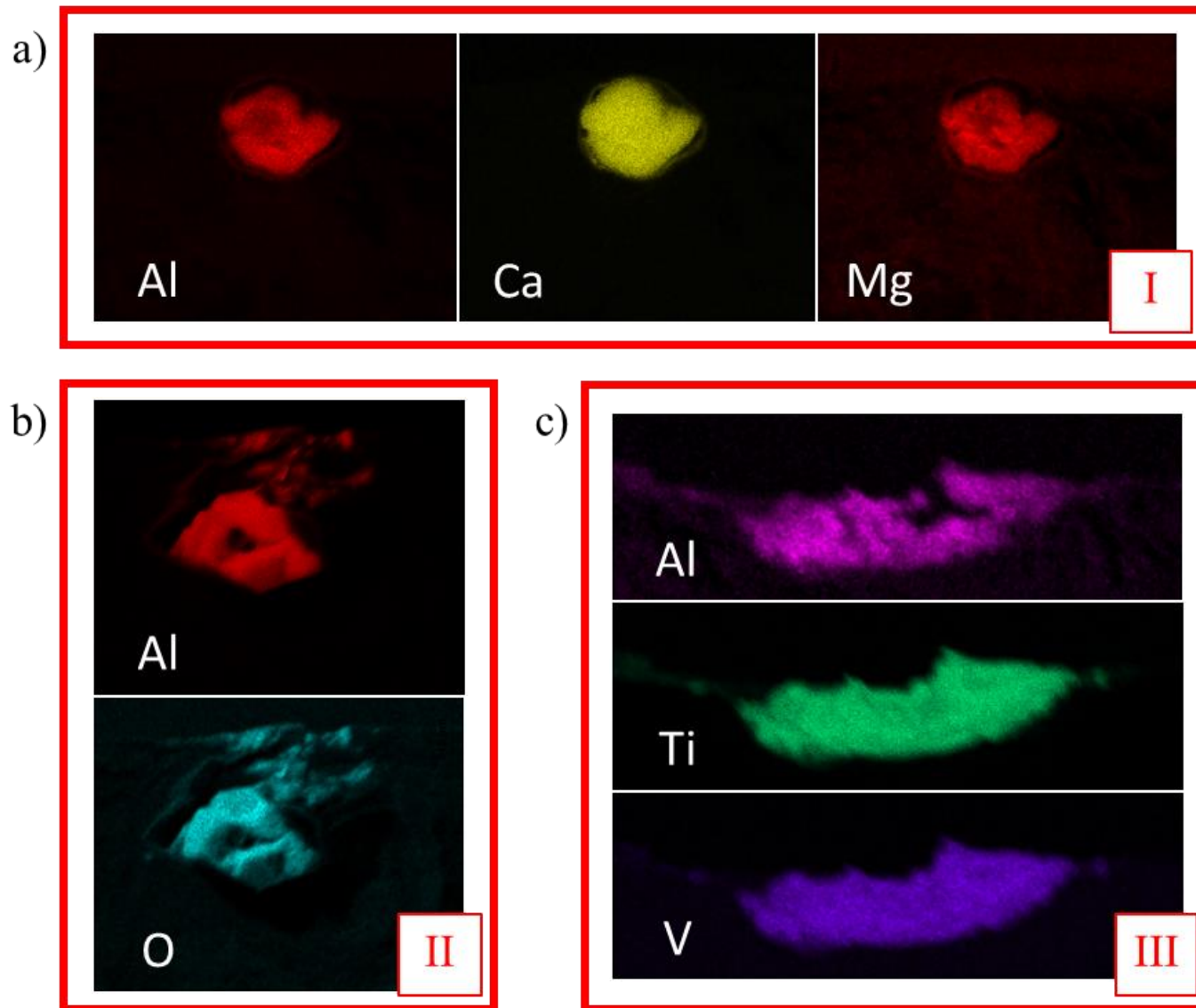


782

783

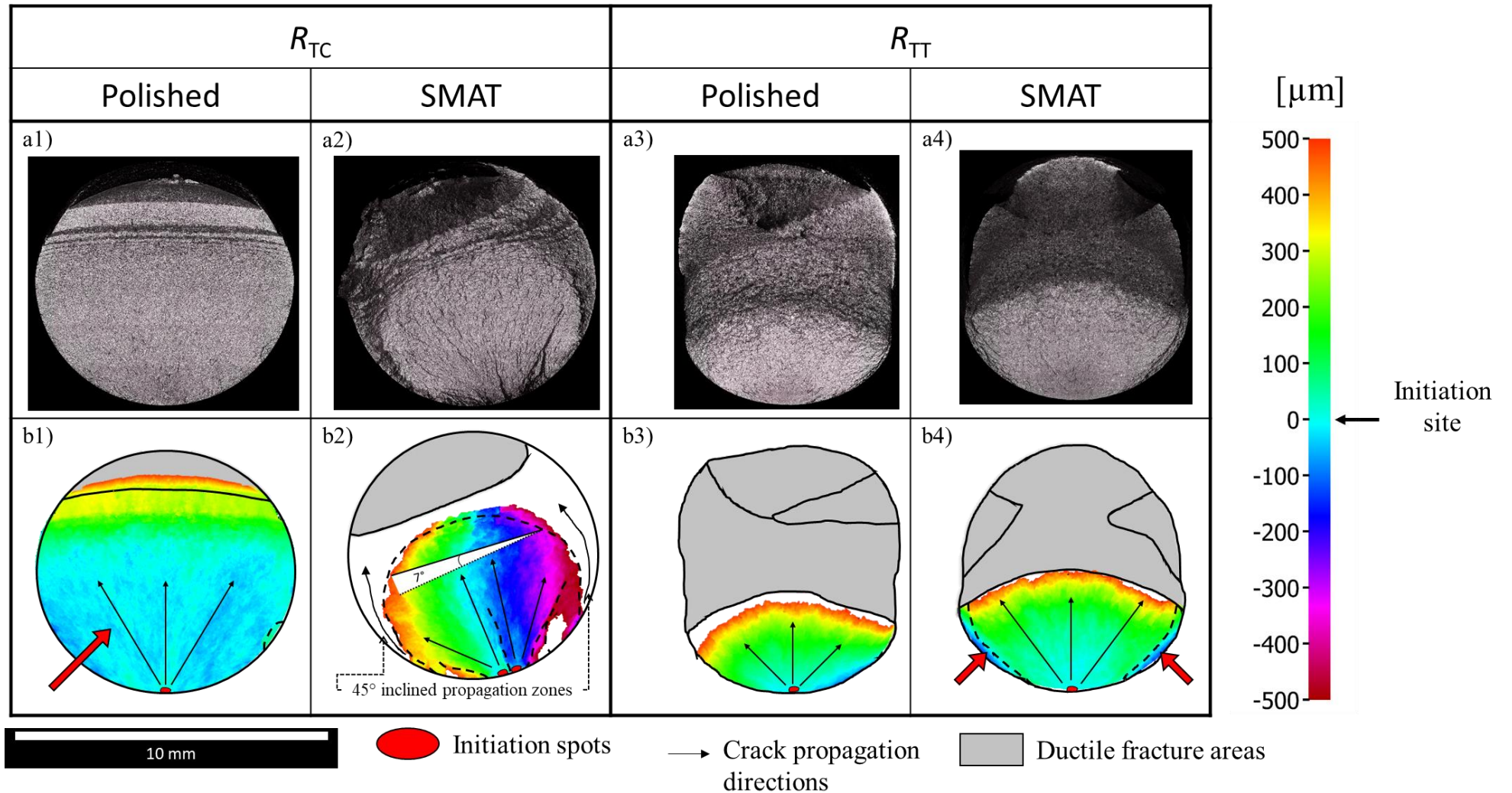
784

Figure 2 SEM images of the characteristic initiation sites for a)  $R_{TC}$  polished, b)  $R_{TC}$  SMAT, c)  $R_{TT}$  polished, d)  $R_{TT}$  SMAT and e)  $R_{TT}$  SMAT + polished samples for respectively 1) high and 2) low stress amplitudes



785  
786

Figure 3 EDX maps corresponding to the regions highlighted in red in Figure 2



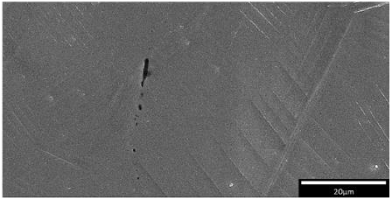
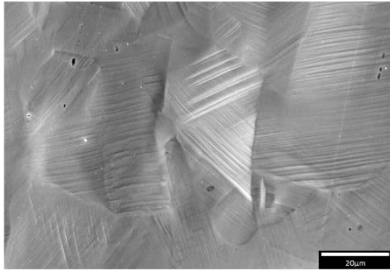
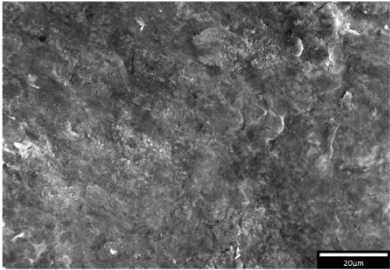
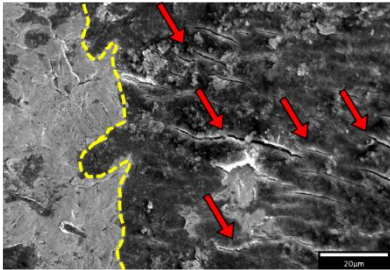
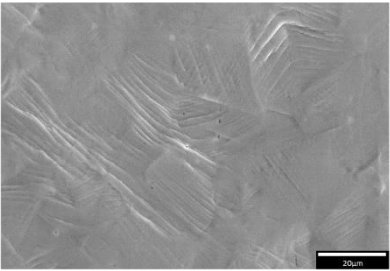
787

788

789

Figure 4 Observations of fracture surfaces a) optical microscope pictures and b) sketches with topology mapping of 1)  $R_{TC}$  polished 210 MPa, 2)  $R_{TC}$  SMAT 245 MPa,

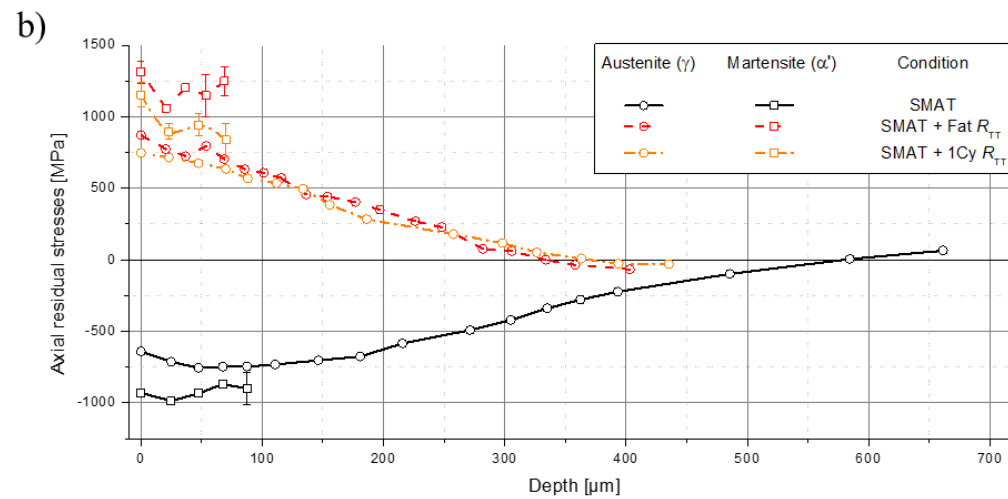
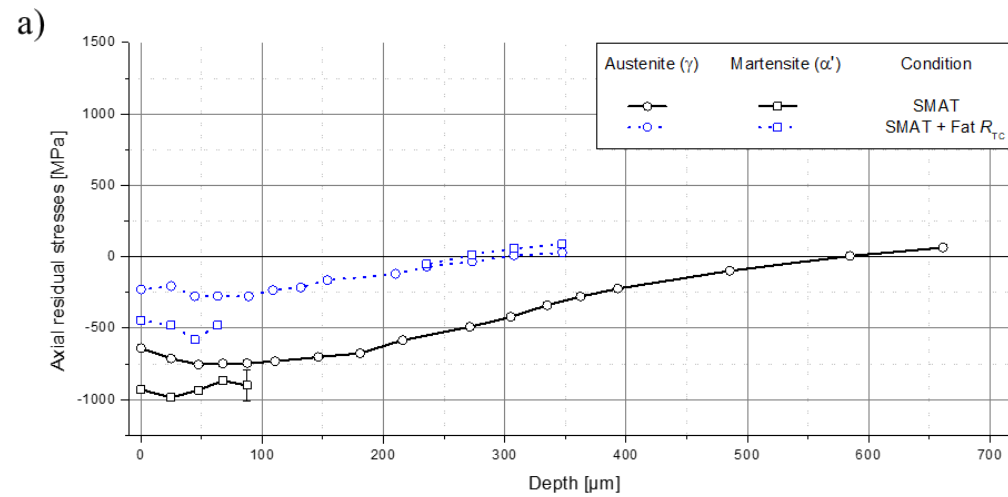
3)  $R_{TT}$  polished 232.5 MPa and 4)  $R_{TT}$  SMAT 220 MPa samples

	$R_{TC}$	$R_{TT}$
Polished	a) 	c) 
SMAT	b) 	d) 
SMAT + polished	/	e) 

790

791

Figure 5 SEM images of the surface of a)  $R_{TC}$  polished, b)  $R_{TC}$  SMAT, c)  $R_{TT}$  polished, d)  $R_{TT}$  SMAT and e)  $R_{TT}$  SMAT + polished run-out samples



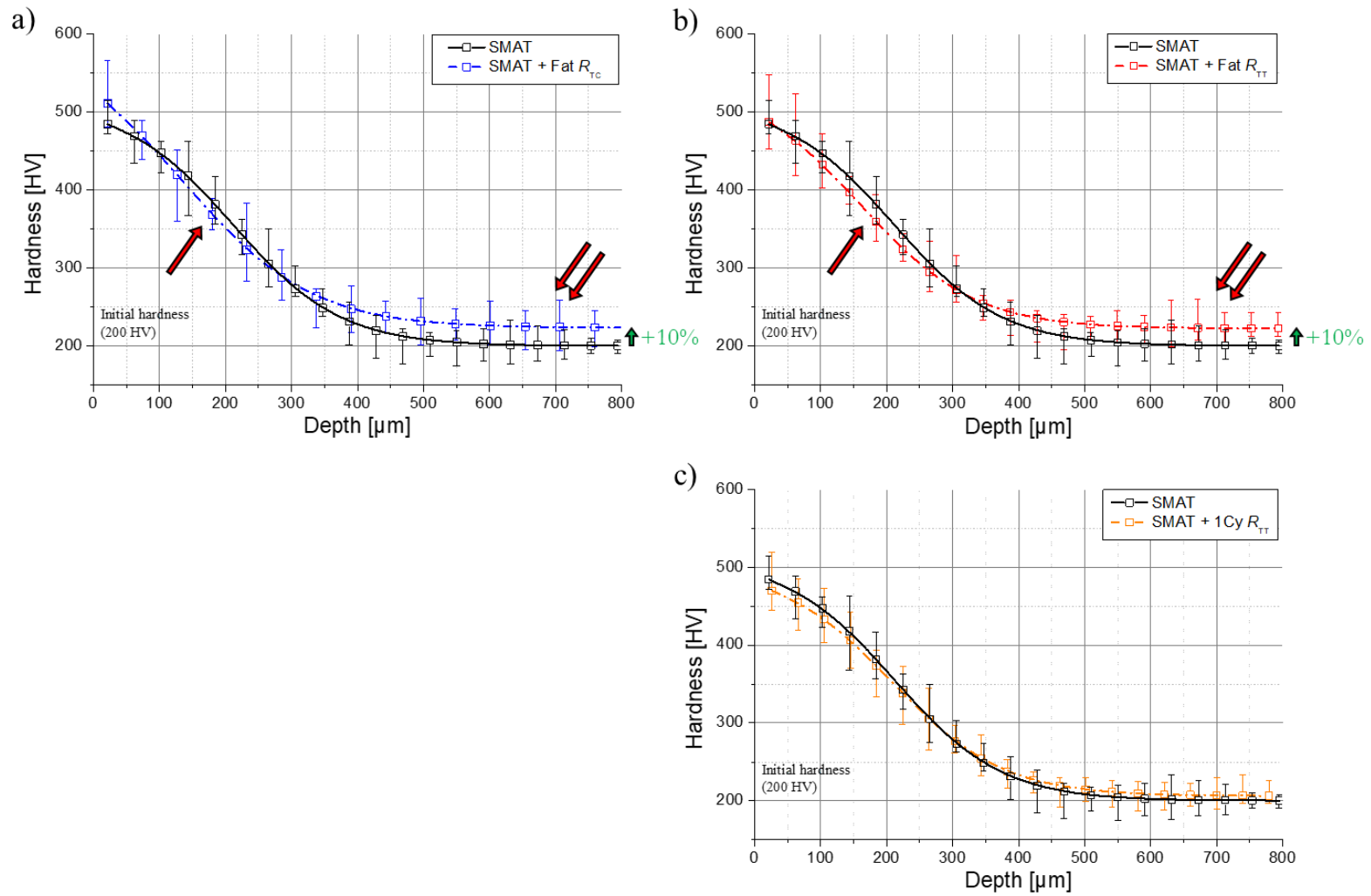
792

793

Figure 6 Evolution of the residual stresses in both austenite and martensite as a function of the depth below the treated surface a) for the SMAT + Fat  $R_{TC}$  condition and

794

b) for the SMAT + Fat  $R_{TT}$  and SMAT + 1Cy  $R_{TT}$ , conditions compared to the SMAT gradient

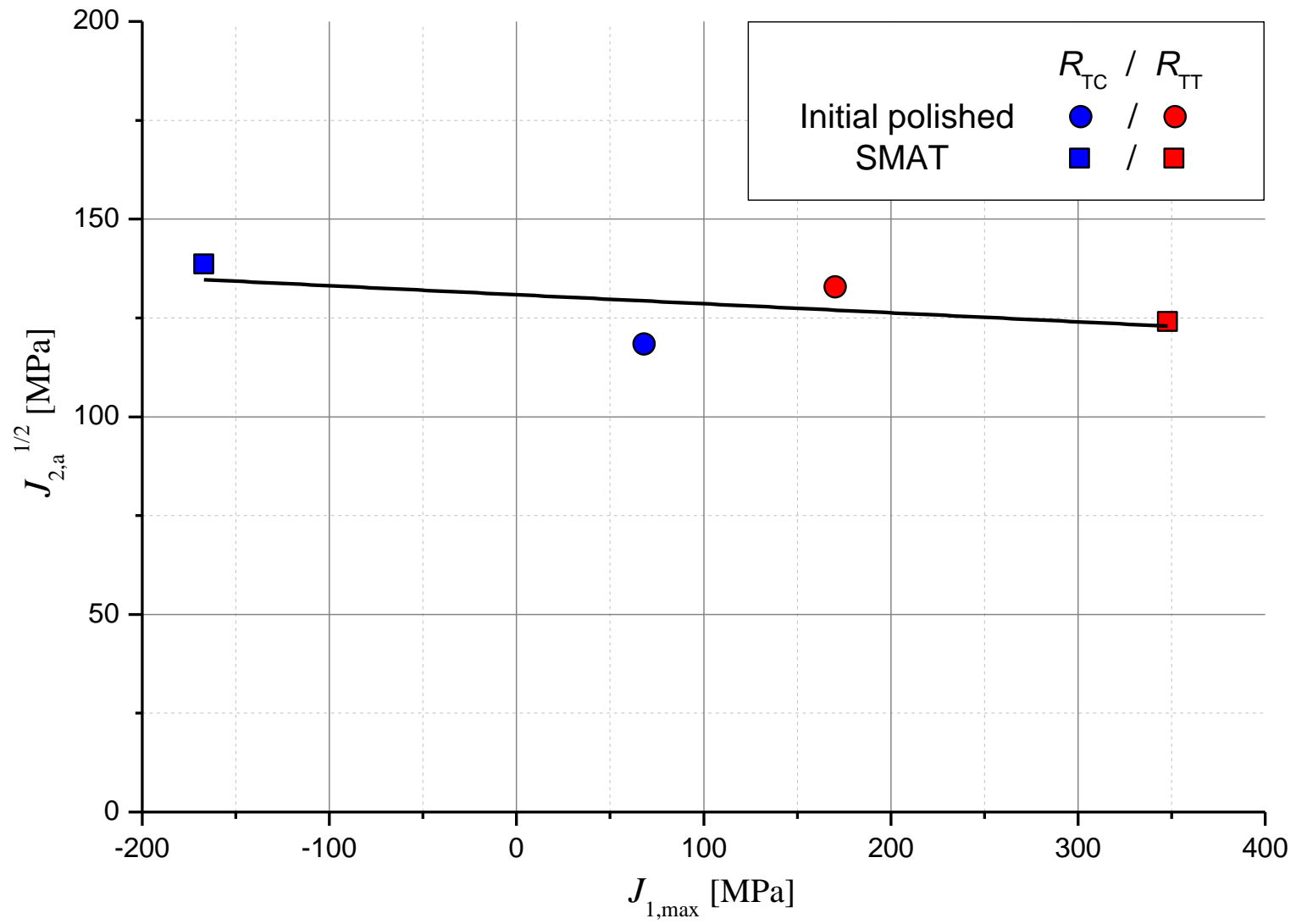


795

796 *Figure 7 Evolution of hardness as a function of the depth below the treated surface after a) SMAT + Fat  $R_{TC}$ , b) SMAT + Fat  $R_{TT}$  and c) SMAT + 1Cy  $R_{TT}$ , compared to*

797

*the SMAT gradient*



798

799

Figure 8 Crossland criterion established for all the tested load ratios and surface states